AGU PUBLICATIONS

JGR

Journal of Geophysical Research: Atmospheres

RESEARCH ARTICLE
10.1002/2013JD021424

Key Points:
- Multisensor satellite-simulator-based evaluation
- Interpretation of satellite radiance and backscatters
- Uniqueness, advantages, and disadvantage of radiance-based evaluation

Correspondence to:
T. Matsui,
Toshihisa.Matsui-1@nasa.gov

Citation:
Matsui, T., et al. (2014), Introducing multisensor satellite radiance-based evaluation for regional Earth System modeling, *J. Geophys. Res. Atmos.*, *119*, 8450–8475, doi:10.1002/2013JD021424.

Received 24 DEC 2013
Accepted 12 JUN 2014
Accepted article online 21 JUN 2014
Published online 15 JUL 2014

Introducing multisensor satellite radiance-based evaluation for regional Earth System modeling

T. Matsui[1,2], J. Santanello[1], J. J. Shi[1,3], W.-K. Tao[1], D. Wu[1,4], C. Peters-Lidard[1], E. Kemp[1,4], M. Chin[1], D. Starr[1], M. Sekiguchi[5], and F. Aires[6]

[1]NASA Goddard Space Flight Center, Greenbelt, Maryland, USA, [2]Earth System Science Interdisciplinary Center, University of Maryland, College Park, Maryland, USA, [3]Goddard Earth Sciences Technology and Research, Morgan State University, Baltimore, Maryland, USA, [4]Science Systems and Applications, Inc., Lanham, Maryland, USA, [5]Faculty of Marine Technology, Tokyo University of Marine Science and Technology, Tokyo, Japan, [6]Estellus, Paris, France

Abstract Earth System modeling has become more complex, and its evaluation using satellite data has also become more difficult due to model and data diversity. Therefore, the fundamental methodology of using satellite direct measurements with instrumental simulators should be addressed especially for modeling community members lacking a solid background of radiative transfer and scattering theory. This manuscript introduces principles of multisatellite, multisensor radiance-based evaluation methods for a fully coupled regional Earth System model: NASA-Unified Weather Research and Forecasting (NU-WRF) model. We use a NU-WRF case study simulation over West Africa as an example of evaluating aerosol-cloud-precipitation-land processes with various satellite observations. NU-WRF-simulated geophysical parameters are converted to the satellite-observable raw radiance and backscatter under nearly consistent physics assumptions via the multisensor satellite simulator, the Goddard Satellite Data Simulator Unit. We present varied examples of simple yet robust methods that characterize forecast errors and model physics biases through the spatial and statistical interpretation of various satellite raw signals: infrared brightness temperature (Tb) for surface skin temperature and cloud top temperature, microwave Tb for precipitation ice and surface flooding, and radar and lidar backscatter for aerosol-cloud profiling simultaneously. Because raw satellite signals integrate many sources of geophysical information, we demonstrate user-defined thresholds and a simple statistical process to facilitate evaluations, including the infrared-microwave-based cloud types and lidar/radar-based profile classifications.

1. Introduction

A mesoscale meteorological model is a practical tool to conduct regional weather and air pollution forecasts and to study important mesoscale weather phenomena, such as hurricanes, squall lines, thunderstorms, and various types of tropical convection interacting with land and ocean processes [*Pielke*, 2013]. Due to recent increases of computational power, more comprehensive mesoscale models have been developed capable of simulating cloud-precipitation, aerosols, and land surface processes down to the storm-resolving scale (1–5 km horizontal grid spacing) [*Cotton et al*., 2003]. The largest advantage of this fine-resolution modeling is that atmospheric convective processes are realistically depicted by the dynamical core instead of using a cumulus convection scheme [*Tao and Moncrieff*, 2009; *Weisman et al*., 1997]. Since scales of these simulated mesoscale phenomena are also comparable to modern Earth-observing satellite measurements, various physical processes can be conceivably evaluated against various modern satellite observations, linking to various aspects of clouds, precipitation, aerosols, and land surface characteristics [*Parkinson*, 2003; *Simpson et al*., 1996; *Schoeberl et al*., 2006].

However, multisatellite and multiinstrumental measurements have also revealed uncertainties among different satellite products. For example, different visible infrared (IR) sensors, microwave sensors, lidar, and cloud radar can retrieve cloud ice-water contents, which can be substantially different from each other due to different retrieval methods and/or different satellite instrument platforms [*Roebeling et al*., 2013; *Waliser et al*., 2009]. In a specific rainfall regime, precipitation estimates from satellite precipitation radar, cloud profiling radar, and passive microwave sensors can have large discrepancies [*Berg et al*., 2008]. Depending on the choice of the near-infrared channels, estimation of cloud top effective radius yields different results due to different sensitivities to the presence of drizzle droplets near the cloud top [*Chang and Li*, 2003; *Nakajima*

et al., 2010]. Even using the same sensor channels, the variety of retrieval methods and their physical assumptions result in different aerosol optical depths [*Myhre et al*., 2004].

Satellite retrievals always face a fundamental problem: the number of uncertainties that characterize satellite-observable electromagnetic signals exceeds the number of satellite-received signals. This requires satellite retrievals to make unique assumptions to estimate the geophysical parameters from space. While retrieved geophysical parameters are useful to quantify geophysical parameters (often called Level 2 and Level 3 data sets), it often frustrates evaluating atmospheric models in detail due to different physical assumptions between various satellite retrievals and Earth System models [*Eliasson et al*., 2011; *Waliser et al*., 2009].

One of the alternative approaches is to use direct satellite measurements, i.e., calibrated radiance and/or backscatter (often called Level 1 data), for model evaluation. In this approach, a satellite simulator (or a forward model) must be utilized to translate model geophysical parameters into the satellite-observable radiance or backscatters [e.g., *Chaboureau et al*., 2000; *Masunaga et al*., 2008; *Matsui et al*., 2009]. As long as calibration and uncertainties of the satellite sensor are well known, the satellite level 1 data are the most direct observation with neither physical assumptions nor retrieval procedures. If satellite-observable signals are simulated from the model physics assumptions, the radiance-based evaluation possibly allows more apple-to-apple comparison against satellite measurements. Multiple satellite measurements could reveal various aspects of the model strengths and weaknesses.

For example, *Han et al*. [2013] used satellite microwave brightness temperature (Tb) and ground-based Doppler radar signals for evaluating different bulk microphysics schemes in the Weather Research and Forecasting (WRF) model. *Hashino et al*. [2013] used satellite radar and lidar signals to evaluate cloud microphysics simulation from a global storm-resolving model. *Li et al*. [2010] used satellite and ground-based precipitation radars and microwave Tb to constrain precipitation microphysics from squall line simulation. *Matsui et al*. [2009] combined satellite-derived infrared Tb, precipitation radar, and microwave Tb to establish a comprehensive evaluation framework for the long-term cloud-resolving model simulations. Similar approaches have been further applied to cloud-precipitation data assimilation framework in regional models [*Vukicevic et al*., 2006; *Polkinghorne and Vukicevic*, 2011; *Zupanski et al*., 2011a; *Zhang et al*., 2013].

Passive microwave and IR Tb have been widely utilized to assess forecasting and model physics in the French mesoscale meteorology research group. *Chaboureau et al*. [2000] utilized Meteosat Tb from IR and water vapor channels to evaluate forecast skill of the Meso-Nonhydrostatic (Meso-NH) model with a forward model. Their study is one of the pioneering studies that applied "model-to-satellite" approach to a mesoscale model with explicit microphysics scheme. *Chaboureau et al*. [2002] examined a possibility of adjusting model microphysics parameters toward observed radiance through model-to-satellite approach. *Wiedner et al*. [2004] applied passive microwave Tb and a microwave simulator to evaluate simulated deep convection, and *Meirold-Mautner et al*. [2007] examined sensitivity of ice single-scattering properties to simulated microwave Tb. *Söhne et al*. [2006, 2008] applied objective analysis method to the model-to-satellite approach for evaluating cloud cover, and the same technique was applied to evaluate ensemble forecasting skill [*Chaboureau et al*., 2012]. *Chaboureau and Pinty* [2006] utilized two-channel IR Tb techniques to validate cirrus parameterization in the Meso-NH model, and *Chaboureau et al*. [2007] applied the same technique to examine diurnal cycle of cirrus clouds and mineral dust.

This radiance-based evaluation method, however, requires an understanding of the satellite measurements and the underlying physics principles of electromagnetic scattering theory, radiative transfer, and satellite-sensor measurement patterns. Yet there is still a large knowledge gap between the satellite and the modeling communities on these critical topics. Therefore, an introductory but wide-ranging discussion of satellite radiance-based evaluation methods should be addressed especially for regional Earth System modeling community members without solid background of forward modeling and satellite remote sensing.

The major objective of this paper is to introduce unique multisensor radiance-based evaluation methods and principles of regional Earth System models using satellite simulators with a series of examples in simple spatial and statistical analysis. To date, the potential of combining mesoscale model output and multisensor satellite radiance data has been yet largely unrealized. Therefore, section 2 first discusses key principles, philosophy, and advantage/disadvantage of radiance-based evaluation method. Section 3 briefly describes a regional model and a multiinstrument satellite simulator used in this manuscript. A series of examples and interpretation of the satellite measurements are shown in section 4, including discussion of relationship

between geophysical parameters and various satellite signals with emphasis on aerosol-cloud-precipitation-land processes. Section 5 summarizes results and makes conclusion.

While our emphasis is to present simple examples so that diverse modeling communities can readily understand the concept and the utility, we would like to point out that this manuscript does not (i) provide a detailed description of physics and mathematics principles in radiative transfer or scattering theories, which are more completely described in the available textbooks [*Stephens*, 1994; *Liou*, 2002; *Petty*, 2006; *Bohren and Huffman*, 1998]; (ii) provide comprehensive evaluation results using ensemble simulations or various cases studies over different seasons and/or climate regimes; and (iii) achieve specific improvements of model physics or modules in comparison with observations, as such efforts are covered in other papers, e.g., for cloud microphysics [e.g., *Chaboureau et al*., 2002; *Iguchi et al*., 2012; *Li et al*., 2010; *Lang et al*., 2011], for land surface [e.g., *Matsui et al*., 2007], and for aerosols [e.g., *Petrenko et al*., 2012; *Cheng et al*., 2008] to note a few.

2. Principles and Philosophy of Radiance-Based Model Evaluation

First of all, key advantages, recommendations, limitations, and uncertainties of radiance-based evaluations are discussed. These principles are basics but very important for those who utilize multisensor satellite simulators for their mesoscale modeling studies.

The most significant advantages of the satellite radiance-based evaluation include

1. *Radiance-based evaluations avoid retrieval assumptions and uncertainties inherent in satellite-retrieved products, and thereby provide apple-to-apple comparisons between models and observations*. Satellite-observed and well-calibrated radiance or backscattering data are the most direct observations without any problem of inverse model in retrievals.
2. *Radiance-based approaches could allow evaluating detailed aspects of model assumptions or simulations, such as cloud and aerosol microphysics and land surface characteristics by carefully analyzing simulated radiance fields*. This is because one can use model's physics assumption within a forward model to diagnose sensitivity of simulated radiance to the observed radiance.
3. *Modelers can also investigate impact of forward model uncertainties, which inherently exist in the satellite retrieval algorithm*. Often, there are larger uncertainties in calculating land surface emissivity or single-scattering assumptions at a particular wavelength or frequency, which often biases satellite-derived products. With satellite simulator, one can examine such uncertainties through diagnosing simulated radiance.

While radiance-based evaluation has large potential and various advantages in the situations discussed above, disadvantages and limitations must be also addressed here:

1. *Radiance-based evaluation requires substantial background knowledge to interpret radiation and backscatter fields*. As explained in later sections, interpretation of satellite-raw radiance fields requires basic and/or advanced knowledge of satellite instruments, radiative transfer, and single-scattering theory. While this manuscript address several basics, we encourage the modeling community to learn more fundamentals from available textbooks [*Liou*, 2002; *Petty*, 2006; *Bohren and Huffman*, 1998; *Ulaby et al*., 1981; *Stephens*, 1994]. Various journal publications, including this manuscript, of satellite remote sensing are also a good source to learn key channels, sensors, and techniques relating to geophysical parameters.
2. *Radiance interpretation often varies in different seasons and over different climate regimes*. This is especially true for passive instruments, e.g., visible IR and microwave radiometers as background atmosphere-land surface properties changes. E.g., separation of cloud and land surface IR Tb is relatively easy over tropics but would be difficult over high-latitude regions. Low-frequency microwave Tb drastically changes between land and ocean surface. Alternatively, satellite-retrieved products reasonably take account background variability of radiance in the algorithms.
3. *Visible radiance fields are also affected by satellite sensor scanning and solar angles*. For a given atmospheric column, satellite sensor viewing angle, solar zenith angle, and solar-view cone angles provide variability of simulated and observed radiances. This could frustrate the application of simple radiance-based evaluation methods to visible imager observations, and examples are not shown in this introductory manuscript. However, it is possible to utilize such channels to evaluate clouds or aerosol fields [e.g., *Weaver et al*., 2007], as long as additional parameters (e.g., sensor-solar angles and surface reflectance) are properly treated in the evaluation methods.

4. *Radiance fields are affected by multiple geophysical parameters*. Thus, it often creates confusion for evaluating a specific geophysical parameter. However, this can be advantageous for evaluating Earth System modeling, since radiance-based evaluation allows more complete assessment related to multiple geophysical parameters. For example, cloud fraction and types (altitude) and surface skin temperature must be reasonably simulated by a mesoscale model in order to accurately simulate IR Tb of window channels. In order to simulate accurate lidar backscattering, a mesoscale model must accurately simulate aerosols and clouds profiles.
5. Single radiance/backscatter information often results in nonsingularity issue in interpreting model-observation differences related to a specific geophysical parameter. For example, a combination of low clouds and thin cirrus create similar IR Tb to midlayer clouds [e.g., *Chang and Li*, 2005]. This limitation also applies to single-channel satellite retrievals, too. Well-designed multichannel multisensor evaluation approach could overcome this issue.

For given advantages and disadvantages, readers may consider using direct radiance/backscatter data in lieu of satellite-derived products (a) when a satellite product presents large variability among different retrieval techniques, or across different satellite platforms; (b) when physical assumptions in satellite retrievals are critically different from model assumptions; or (c) when a modeler aims to evaluate a very detailed level of model physics evaluation, beyond retrieval uncertainty level. In these cases, we also provide the following recommendations to derive maximum benefit from the radiance-based evaluation approach:

1. Quality of the forward model in a satellite simulator should be close to those used for satellite remote sensing retrievals.
2. Physical assumptions and model diagnostic and prognostic parameters must be treated as consistently as possible in a forward model.
3. Diverse signal data from satellite instruments and channels should be used simultaneously for more comprehensive evaluations across coupled model components while avoiding nonsingularity issue.

Having addressed these advantages/disadvantages and recommendation, various multisensor radiance-based model evaluation approaches are reviewed with the specific examples in the following sections.

3. Modeling Systems

This study uses the NASA-Unified Weather Research and Forecasting (NU-WRF) model (https://modelingguru.nasa.gov/community/atmospheric/nuwrf). The objective of the NU-WRF is to develop a regional Earth System modeling and assimilation system on the satellite resolvable scale. NU-WRF has been developed at NASA and is based upon the WRF-Advanced Research WRF (ARW) model [*Skamarock et al*., 2008] and WRF-Chem [*Grell et al*., 2005]. The NU-WRF has the wider capabilities of Goddard physics packages (aerosols, cloud, and radiation interactions), land surface modeling and assimilation (NASA Land Information System) [*Peters-Lidard et al*., 2007], and a satellite simulator over the WRF-ARW.

This manuscript utilizes the NU-WRF simulation from *Shi et al*. [2013] that features a specific Mesoscale Convective System (MCS) interacting with land and aerosols (mineral dust) processes over West Africa coincide with the African Monsoon Multidisciplinary Analyses (AMMA) experiments. As a demonstration of the radiance-based evaluation method, we primarily focus on the simulation results at 01 Z 6 August 2006, because of the maturity of the simulated MCS surrounded by mineral dust and the coinciding of these features with various satellite observations. This particular NU-WRF simulation uses three nested domains (two inner nests) with two-way nesting (i.e., the outer domain provides lateral boundary conditions for the inner domain, and results from an inner domain are averaged over the outer domain). Horizontal grid spacings of the middle and the inner domains are 6 km and 2 km, respectively, to resolve mesoscale dynamics associated with fine-scale aerosol-cloud-precipitation-land interactions [*Shi et al*., 2013]. This manuscript focuses on evaluating the middle domain using the satellite data, which has fairly large-scale areal coverage close to the swath widths of satellite passive sensors.

The G-SDSU is an end-to-end multisatellite and multiinstrument simulator and is designed to support meso-γ-scale atmospheric models [*Matsui et al*., 2013]. It has been developed upon the Hydrospheric Atmospheric Research Center (HyARC) SDSU through the collaborations of the various universities and institutions [*Masunaga et al*., 2010]. The G-SDSU includes satellite orbit-scanning geolocation calculations,

generalized single-scattering databases/calculations, and various radiative transfer models (RTMs) that can be applied to most of the existing satellite sensors. Most of the RTMs have been previously applied to construct various remote sensing algorithms [*Nakajima et al*., 1991; *Higurashi and Nakajima*, 1999; *Dubovik and King*, 2000; *Kummerow et al*., 2001; *Masunaga and Kummerow*, 2006; *Olson et al*., 2006]. The particle size distributions (PSD) of hydrometeors and aerosols are treated with the model (NU-WRF) microphysics assumptions and are nearly identical in various simulator components. All simulators are one-dimensional RTMs that assume a plane-parallel atmosphere. While visible IR simulator assumes column simulation, the microwave and the radar simulators are configured for slant-path (pseudo 3-D) radiative transfer [*Olson et al*., 2006]. The simulated radiances or backscattering signals are convolved in the antenna gain patterns of the instruments through satellite orbit and scanning simulators [*Matsui*, 2013]. More details are described in Appendix A.

4. Satellite Observations and Examples of Simulated L1 Data From NU-WRF

4.1. Aqua Moderate Resolution Imaging Spectroradiometer (MODIS) Infrared Brightness Temperature

Among satellite raw data, the IR window region (8μm to 14μm) is the most familiar "raw radiance" data widely used in the meteorological community. IR Tb emitted from the Earth's surface or from a cloud are used to estimate cloud top temperature [*Inoue*, 1987; *Rossow and Lacis*, 1990; *King et al*., 1992; *Menzel et al*., 2008] or land surface skin temperature [*Price*, 1984; *Wan and Dozier*, 1996; *Mao et al*., 2005] and for evaluation and assimilation of clouds [*Chaboureau et al*., 2002; *Vukicevic et al*., 2006; *Zupanski et al*., 2011b]. IR Tb is available for both daytime and nighttime, while the visible channel is generally available only for daytime. In particular, 11 μm channel has the least molecular absorption and the spatially homogeneous surface emissivity [*Hulley and Hook*, 2011]. Thus, it has been used for wide variety of model evaluation studies [*Morcrette*, 1991; *Chevallier and Kelly*, 2002; *Cintineo et al*., 2014; and others described in section 1]. Recently, operational and forecasting research centers start producing simulated satellite IR images from high-resolution mesoscale modeling, and the simulated satellite fields are available in real time and utilized by forecasters [*Clark et al*., 2012; *Bikos et al*., 2012].

As an example, this study uses IR Tb measurements from the Moderate Resolution Imaging Spectroradiometer (MODIS) aboard the polar-orbiting Aqua satellite. MODIS is the cross-tracking visible IR radiometer with a ±55° wide viewing angle that yields approximately 2400 km swath width. The data used here are the 5 km resolution aggregated L1B product (MYDSH01).

Figure 1a shows the Aqua MODIS (hereafter just denoted as MODIS) band31 (bandwidth 10.780–11.280μm) $Tb_{11\mu m}$ observations over the AMMA domain (nighttime overpass around local 1 A.M.). A region of very low $Tb_{11\mu m}$ (less than 220 K) centered in the domains represents a MCS. Slightly low Tb (260–270 K) suggests the presence of boundary layer clouds. Moderately low Tb (220–260 K) could represent midlayer clouds or boundary layer clouds overlapped by thin cirrus clouds. High Tb (exceeding 280 K) generally represents surface skin temperature.

MODIS-observable $Tb_{11\mu m}$ is computed by the G-SDSU visible IR simulator (R-STAR Version 6b, http://157.82.240.167/~clastr/dl/rad.html) through a discrete-ordinate radiative transfer scheme [*Nakajima and Tanaka*, 1986, 1988; *Stamnes et al*., 1988]. Satellite swath and local incidence angle are estimated from satellite orbit and sensor scan module [*Matsui*, 2013] that accounts for the Aqua satellite orbit and the MODIS cross-track scanning.

The three-dimensional atmospheric state (pressure, temperature, humidity, and height), particles/drops (aerosol, cloud, and precipitation), and surface state (skin temperature) at 01 Z 5 August 2006 are used to simulate MODIS $Tb_{11\mu m}$. Figure 1b shows simulated MODIS $Tb_{11\mu m}$, which features a region of very low $Tb_{11\mu m}$ (less than 220 K) around the center of the domain, representing the impact of the simulated MCS. Note that the MCS is simulated by the inner domain ($dx = dy = 2$ km) in order to resolve cloud dynamics within the MCS. In comparison with the observations (Figure 1a), the simulated MODIS scene does not feature widespread moderately low $Tb_{11\mu m}$ (220–280 K) in the domain, especially over the southeast region.

For simple quantitative metrics, spatial and statistical evaluations are useful standard methods for model evaluation [e.g., *Söhne et al*., 2008; *Chaboureau et al*., 2012]. Spatial evaluation is based on the difference in $Tb_{11\mu m}$ between the observation and the simulation in the identical map coordinate (Figure 1c). It simply and clearly presents biases in location and magnitude of $Tb_{11\mu m}$ associated with the locations of MCSs or

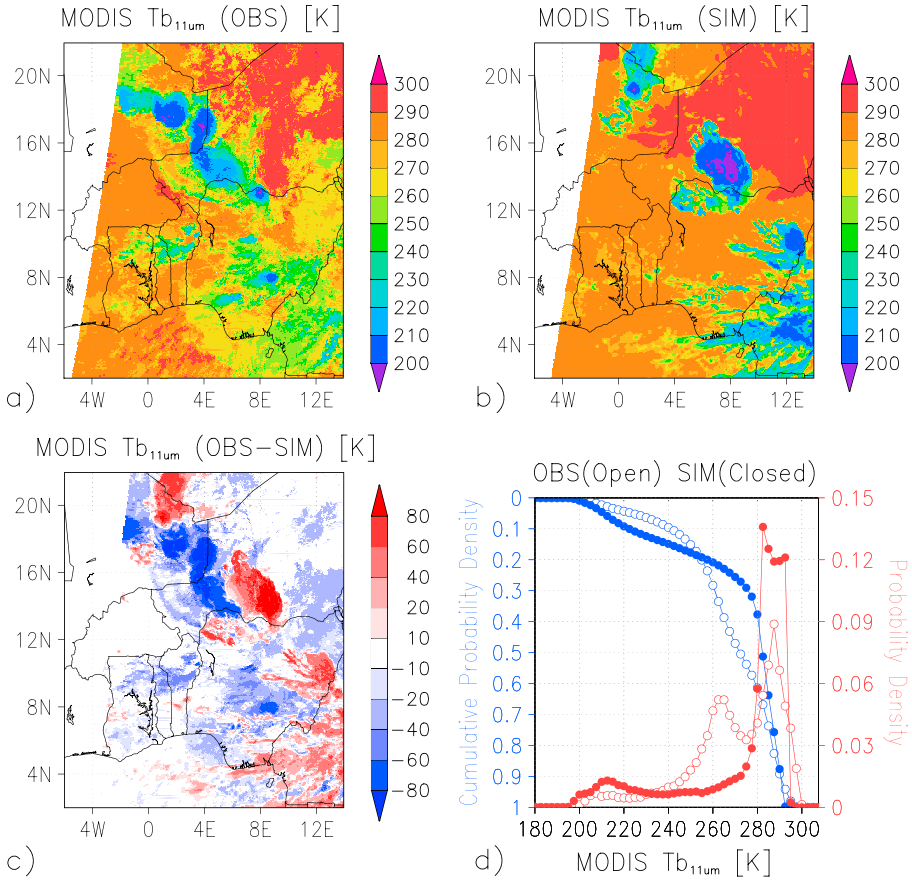

Figure 1. (a) Observed and (b) simulated Aqua MODIS brightness temperature [°K] at 11μm ($Tb_{11\mu m}$) over AMMA domain at 01 Z 6 August 2006. (c) Spatial difference in MODIS Tb between simulation and observation for the same period. Spatial correlation is 0.26. (d) Probability density (both normal and cumulative) of MODIS $Tb_{11\mu m}$.

high cloud cover ($|dTb_{11\mu m}|$ greater than 40 K) and middle/low/overlap cloud cover in the NU-WRF simulations ($|dTb_{11\mu m}| = 10–40$ K). To the first order, spatial evaluation in $Tb_{11\mu m}$ is quite a useful metric for assessment of the weather forecasting quality of cloudiness for mesoscale modeling, which is often related to the errors in initial atmosphere-land conditions and lateral boundary forcing. Therefore, the spatial $Tb_{11\mu m}$ evaluation could be further incorporated into the cloudy affected radiance assimilation for mesoscale models [*Zupanski et al.*, 2011b; *Polkinghorne and Vukicevic*, 2011; *Vukicevic et al.*, 2006; *Seaman et al.*, 2010]. Another unique approach is a time series objective verification of cloud cover through IR and microwave Tb for deterministic forecasting [*Söhne et al.*, 2008] and for ensemble forecasting [*Chaboureau et al.*, 2012].

The statistical evaluation is useful for assessment of the model physics biases within the domain [e.g., *Chaboureau et al.*, 2002; *Grasso and Lindsey*, 2011]. Normalized histograms (probability density) of the MODIS $Tb_{11\mu m}$ are constructed from the MODIS observations and the G-SDSU simulations (Figure 1d). First, we discuss relative frequencies between the observed (red open circles) and simulated (red closed circles). Between 200 K and 240 K in $Tb_{11\mu m}$, the simulation overestimates relative frequencies against the observed frequencies, reflecting the overestimation of high cloud cover or its optical thickness in the domain. For the $Tb_{11\mu m}$ ranges from 240 K to 280 K, the simulation underestimates relative frequencies, suggesting that the NU-WRF simulation could underestimate middle/low/overlap cloud cover. For $Tb_{11\mu m}$ higher than 280 K, the simulation overestimates the relative frequencies, suggesting that the simulation tends to have more areas of noncloudy pixels in the domain, compared to the MODIS observations. It probably requires careful modification of cloud droplets evaluation in subsaturated environment in order to mimic thin planetary boundary layer (PBL) clouds in the continental environment at this grid resolution, since PBL clouds are not well resolved at this resolution.

Cumulative histograms can be used to emulate the cloud areal cover in the domain (Figure 1d). Often, assessment of areal fraction of cloud cover is always arguable, as cloud fraction varies among different satellite products due to sensor resolutions, cloud detection algorithms, and satellite orbiting patterns. Here the simple yet robust Tb coverage method is addressed. Assuming the presence of cloudy pixel based on a threshold of $Tb_{11\mu m}$ of 273 K, the cumulative histograms suggest that domain coverage of cloud fraction is 0.5 in the observation and 0.3 in the simulation (Figure 1d). If one reduces the threshold from 273 K (Tb emitted from low-middle-high clouds) down to 255 K (Tb emitted only from middle to high clouds), the simulation underestimates the total domain cloud fraction; on the other hand, if we further reduce the threshold $Tb_{11\mu m}$ from 255 K down to 220 K (Tb emitted only from high clouds), the simulation overestimates the domain cloud fraction. By looking at all $Tb_{11\mu m}$ threshold spectrum, we can evaluate cloud coverage at different levels: the simulation overestimates (underestimates) high cloud (middle/low/overlap cloud) cover. Although this method is very simple, cloud cover can be defined by modelers with threshold of $Tb_{11\mu m}$ and remain consistent between the simulation and the observations [e.g., *Morcrette*, 1991; *Chaboureau et al*., 2000; *Keil et al*., 2003; *Otkin et al*., 2009].

With proper initial conditions and after a sufficient spin-up period, simulation biases appearing in both relative and cumulative frequencies in this analysis are usually related to the model physics and dynamics in a particular thermodynamics environment rather than the uncertainties in the initial/boundary conditions, while often separating the issue of forecasting error in the MCS location. For example, the middle/low/overlap cloud underestimation in the NU-WRF could be due to misrepresentations in cloud microphysics, PBL mixing, atmospheric heating due to mineral dust aerosols (discussed later), and/or the model horizontal and vertical resolutions.

Besides using satellite simulators, we want to verify a more traditional approach to determine cloud top temperature (T_{CT}) in comparison with satellite-derived T_{CT} product. Traditionally, when comparing satellite-derived T_{CT}, modeler often use the air temperature at the highest cloudy grid level based on an arbitrary threshold of total cloud mass concentration (sum of ice and cloud droplets). In this approach, the definition of "cloudy" grid level depends on the threshold values of total cloud mass concentration. Figure 2 demonstrates the differences between $Tb_{11\mu m}$ and T_{CT} from three different thresholds of cloud mixing ratio. Figure 2 (top) shows the spatial differences, while Figure 2 (bottom) shows scatterplots. We will briefly examine the feasibility of the traditional method by comparing with the simulator-generated $Tb_{11\mu m}$ and identify the relationship between them.

The strictest threshold ($q_{thresh} = 0.0001$ g m^{-3}) overestimates cloudy pixels, and, consequently, the T_{CT} becomes significantly lower than the $Tb_{11\mu m}$ over the southern part of the domain, featuring thin cirrus clouds. Scatterplots suggest differences increase up to 100 K. With the moderate threshold ($q_{thresh} = 0.001$ g m^{-3}), overestimation of cloudy pixels is reduced in the domain, and $T_{CT} - Tb_{11\mu m}$ differences lessens to 70 K in the scatterplots. The largest threshold ($q_{thresh} = 0.01$ g m^{-3}) underestimates most of the thin cirrus and cumulus pixels over south of the domains and pixels around the edge of the MCSs, and the scatterplots show that the T_{CT} becomes significantly higher than the $Tb_{11\mu m}$ (~80 K). Over cloudless pixels (upper central portion of the domain), T_{CT} (surface skin temperature) is up to 10 K higher than $Tb_{11\mu m}$, since the simulated $Tb_{11\mu m}$ is reduced from surface skin temperature due to small effect of surface emissivity and molecular absorption. The scatterplots of all three thresholds (and other thresholds not shown here) show large discrepancies between T_{CT} and $Tb_{11\mu m}$. This simple exercise demonstrated that traditional method for determining T_{CT} is not consistent to the simulated $Tb_{11\mu m}$, which is the major channel that determines T_{CT} in the satellite retrieval algorithm [*Rossow and Schiffer*, 1991].

Another application of using $Tb_{11\mu m}$-based model evaluation is addressed with geostationary satellite measurements. Unlike polar-orbiting satellites, a geostationary satellite allows evaluation of $Tb_{11\mu m}$ at finer temporal resolution including diurnal cycles [*Morcrette*, 1991; *Söhne et al*., 2008; *Otkin et al*., 2009; *Grasso et al*., 2010; *Cintineo et al*., 2014]. For example, *Söhne et al.* [2008] used 3-hourly Meteosat Tb to evaluate the quality of model forecasts of cloud cover in the AMMA framework. The data used in this study are the merged IR product, which combines all available IR window Tb from different geostationary satellites and empirically corrects for viewing angle effects [*Janowiak et al*., 2001]. Figure 3a shows a 2 day time series of $Tb_{11\mu m}$ histograms derived from observations and the NU-WRF simulations.

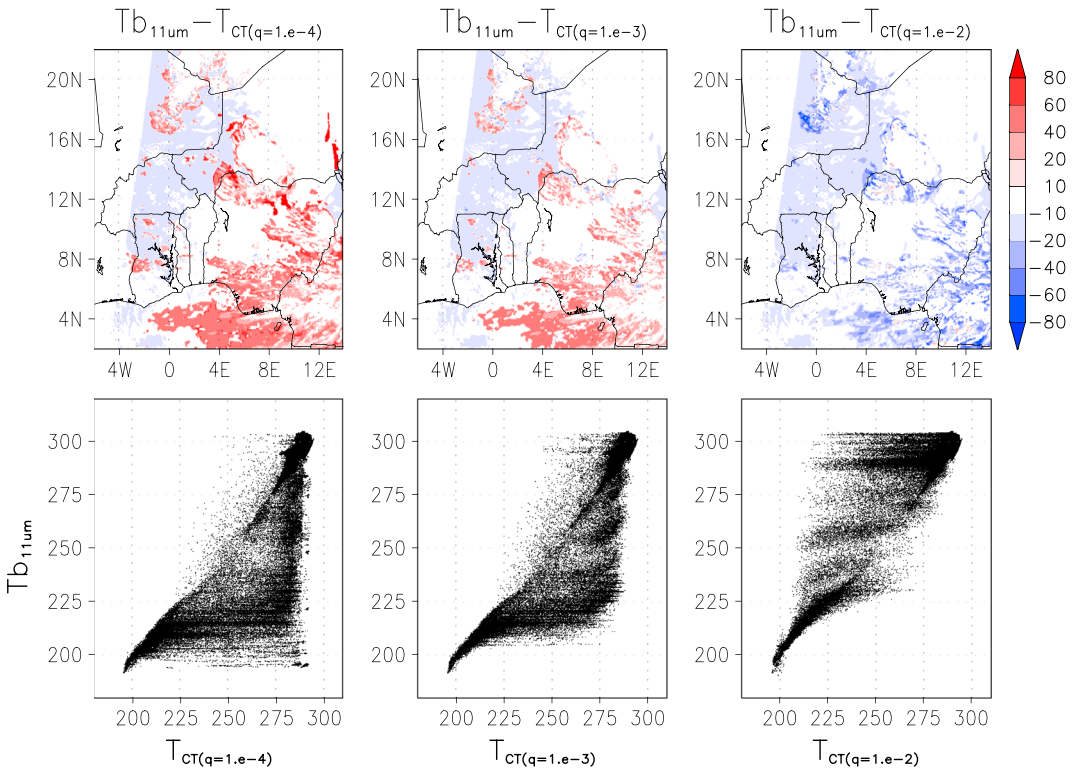

Figure 2. Comparison between simulated MODIS $Tb_{11\mu m}$ and cloud-top temperature (T_{CT}) derived from three different thresholds ($q_{thresh} = 0.0001, 0.001, 0.01$ g m^{-3}). Top panel shows spatial comparison, while bottom panel shows differences in scatter plot diagram.

As discussed in reference to Figure 1d, $Tb_{11\mu m}$ greater than ~280 K approximately represents surface skin temperature in this environment; $Tb_{11\mu m}$ of 260–280 K represents pixels of low clouds, $Tb_{11\mu m}$ of 220–260 K represents pixels of middle or overlapped clouds, and $Tb_{11\mu m}$ lower than 220 K represents pixels of high clouds. Thus, the time series of the $Tb_{11\mu m}$ histogram corresponds with diurnal cycles of cloudiness and surface temperature in the domain (Figure 3a). The observation shows that maximum $Tb_{11\mu m}$ peaks at local solar noon (corresponding to 12 Z), on 5 and 6 August; the skin temperature starts to increase after sunrise (06 Z) and peaks at noon (~12 Z); and after sunset (18 Z), it decreases slowly by IR radiative cooling until the next sunrise. The prevalence of observed low $Tb_{11\mu m}$ (below ~225 K) peaks approximately 6 h after (~18 Z) the peak of the surface skin temperature, suggesting the buildup of deep clouds and cirrus anvils during the late afternoon, while the simulated $Tb_{11\mu m}$ does not exhibit this feature. The NU-WRF simulation captures the initial development of increasing the occurrence of low $Tb_{11\mu m}$ around at 18 Z on 5 August, but the region of low $Tb_{11\mu m}$ is maintained until 18 Z of the next day (6 August); when the low $Tb_{11\mu m}$ increases further. Overall, the NU-WRF simulation appears to capture the afternoon convection properly on 5 August, but the dense high clouds (anvils) persist longer than the observations.

To quantify observation-model differences, a 2 day time series of differences between observed and simulated $Tb_{11\mu m}$ is calculated (Figure 3b). This plot clearly indicates that the simulation overpredicts the pixels with $Tb_{11\mu m}$ of 280–290 K throughout model integration, while it underestimates the pixels with $Tb_{11\mu m}$ greater than 290 K. This illustrates that simulated surface skin temperature is generally lower than the observations for daytime (~10 K) as well as nighttime (~3 K). Underestimation of surface skin temperature has often been reported especially over less vegetated surfaces [*Bosilovich et al.*, 2007] possibly due to misrepresentation of (i) surface heat capacity and/or (ii) turbulent roughness coefficients in the land surface model.

For the time series of $Tb_{11\mu m}$ histograms lower than 280 K, the simulation severely underestimates (red shaded) pixel counts with $Tb_{11\mu m}$ of 250–280 K throughout the simulation integration, while it overestimates (underestimates) pixel counts of low $Tb_{11\mu m}$ less than 250 K for early (later) periods. This physically represents

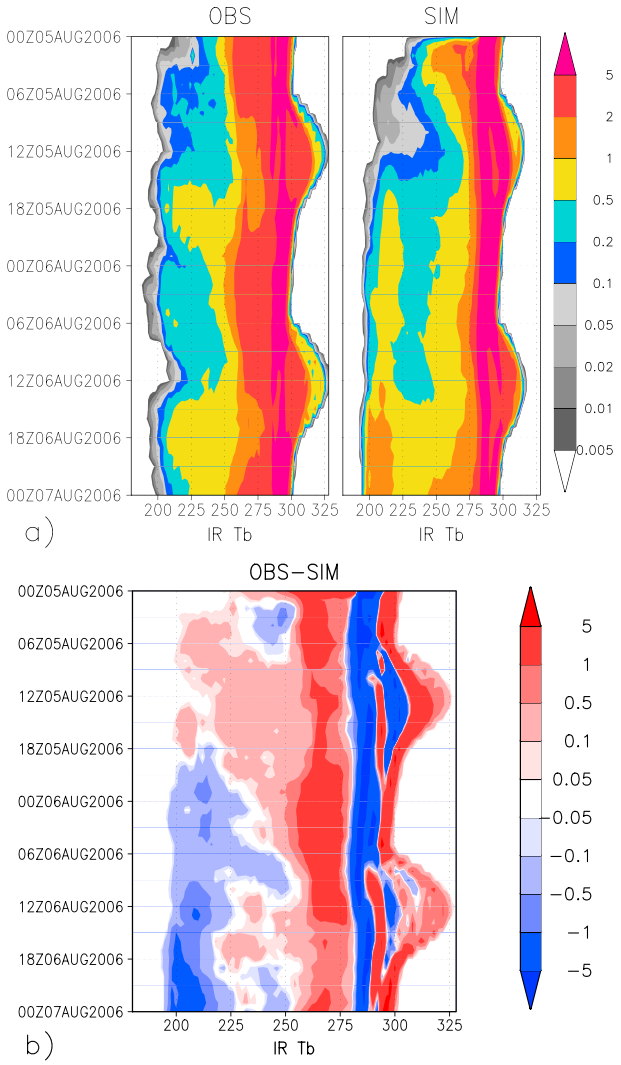

Figure 3. (a) Observed and simulated times series of Geostationary satellite $Tb_{11\mu m}$ histogram. (b) Time series of observation-simulation differences of $Tb_{11\mu m}$ histogram (Both color bars represent frequency in %.).

NU-WRF underestimation of low and midlayer cloud coverage, and overestimation of high clouds in this particular simulation. The underestimation of the high cloud cover during the early periods is attributed to the model spin-up of mesoscale dynamics, while the overestimation of high cloud cover in the later periods is attributed to physics biases in this simulation environment. These conclusions qualitatively agree with the evaluation using the MODIS measurements (Figure 1d) and lend confidence that high temporal resolution analysis using geostationary satellites can effectively reveal diurnal cycles of cloudiness and surface skin temperatures [e.g., *Morcrette*, 1991].

Another interesting channel, not explored in this manuscript, is a water vapor channel (5.7 to 7.1 μm) [e.g., *Chaboureau et al.*, 2000; *Keil et al.*, 2003; *Grasso et al.*, 2010]. With this channel, approximate amount of column water vapor can be evaluated via satellite-observed and simulated Tb. As mentioned, one-channel IR Tb techniques often limit separating midlevel clouds and a combination of low and high cloud cover. In that case, more advanced two-channel IR Tb techniques permit validating cirrus clouds [*Chaboureau and Pinty*, 2006].

4.2. Aqua AMSR-E Microwave Tb

In contrast to the IR window channel described in the previous section, the microwave spectrum is characterized by longer wavelengths (submillimeter to several centimeters) that are generally less sensitive to smaller particles such as aerosols and cloud droplets but more sensitive to large rain drops and large precipitating ice, as well as land surface characteristics. It also has unique sensitivity to water vapor and other gaseous species at some microwave frequencies. As such, passive microwave remote sensing has been applied to various Earth Science applications in studying precipitation, thermodynamics (water vapor and temperature sounding), land surface (soil moisture and flooding), and ocean processes (sea ice, sea surface temperature, and wind speed) [*Ulaby et al.*, 1981].

The Advanced Microwave Scanning Radiometer for Earth Observing System (AMSR-E) is the conically scanning passive microwave imager that senses radiance at six frequency (6.9–89 GHz) with vertical and horizontal polarization [*Kawanishi et al.*, 2003]. The AMSR-E instrument is aboard the Aqua satellite together with the MODIS sensor. In comparison with lower frequency channels, Tb at 89 GHz channel (~3.36 mm wavelength) have higher spatial resolution (instantaneous field of view: $3.5 \times 5.9\ km^2$), is sensitive to the presence of ice aloft associated with deep convection, and is commonly used to detect raining pixels and surface precipitation in the satellite retrieval over land [*Olson et al.*, 2001b]. Thus, high-frequency microwave Tb can be utilized to examine precipitation processes and precipitation microphysics [*Wiedner et al.*, 2004; *Burlaud et al.*, 2007; *Matsui et al.*, 2009; *Li et al.*, 2010; *Gao et al.*, 2011; *Han et al.*, 2013].

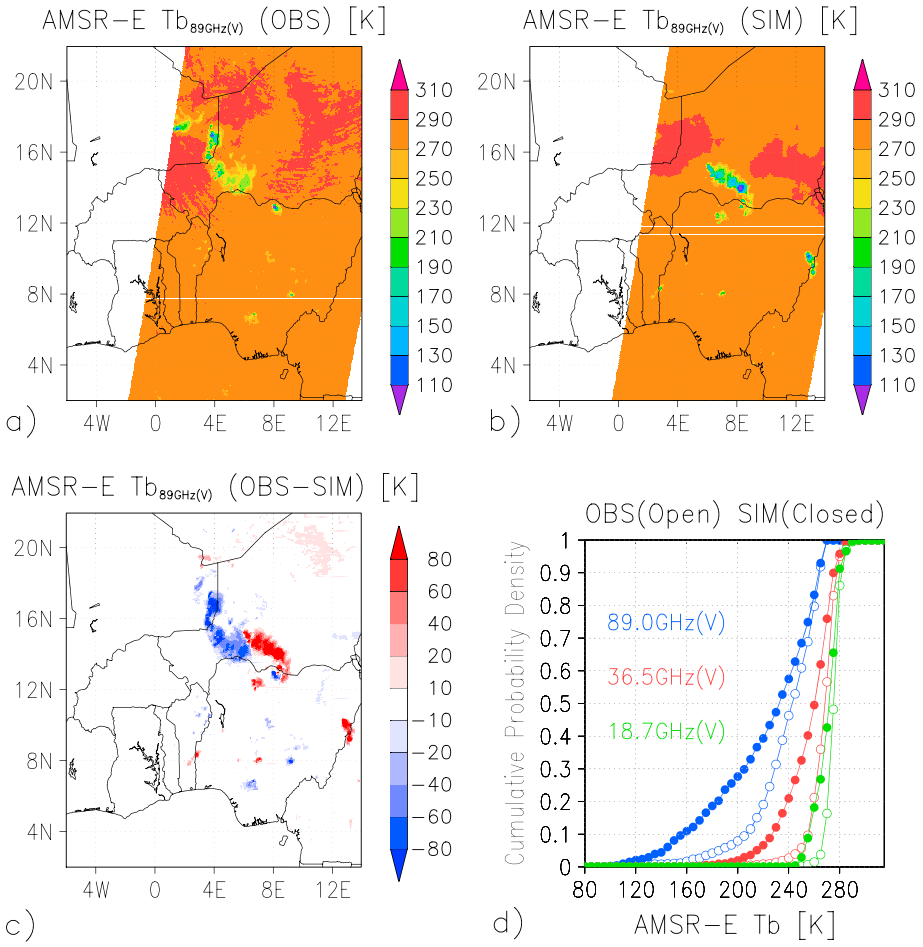

Figure 4. (a) Observed and (b) simulated Aqua AMSR-E brightness temperature (K) at 89 GHz over the AMMA domain around at 01 Z 6 August 2006. (c) Spatial difference in AMSR-E Tb at 89 GHz(V) between simulation and observation for the same period. (d) Cumulative relative frequency histogram of AMSR-E Tb.

Figure 4a shows AMSR-E-observed Tb at 89 GHz(V) over the AMMA domain. There are a couple of large depressions of $Tb_{89GHz(V)}$ consistent with the center of the MCS captured by the MODIS $Tb_{11\mu m}$ (Figure 1a). The presence of significant amount of large ice particles (such as snow aggregate, graupel, or hail) tends to scatter the upwelling surface emission of microwave electromagnetic energy back toward the surface. As a result, top-of atmosphere (TOA) emergent microwave radiance is reduced and appears low. The large-size ice particles settle downward and eventually melt and precipitate. Background $Tb_{89GHz(V)}$ (greater than 270 K) is associated with surface skin temperature and water vapor emission in the lower troposphere. In comparison with the MODIS $Tb_{11\mu m}$ scene (Figure 1a), spatial patterns of $Tb_{89GHz(V)}$ demonstrate no significant sensitivity of $Tb_{89GHz(V)}$ to small cloud particles over the domain.

G-SDSU passive microwave simulator computes TOA emergent microwave Tb by treating two-stream radiative transfer calculations with the Eddington's second approximation along the slant radiance path [*Kummerow*, 1993; *Olson et al.*, 2006; *Matsui et al.*, 2013]. For bottom boundary conditions, wind-induced changes to the water body emissivity at vertical and horizontal polarization are considered over ocean and lake. Over the land surface, an observation-based microwave emissivity database (tool to estimate land-surface emissivities at microwave frequencies (TELSEM)) [*Aires et al.*, 2011] is used to estimate land surface emissivity. In this radiative transfer scheme, horizontal and vertical polarization is considered only at the surface. Rigorous satellite orbit, sensor scanning, and associated antenna gain functions of the AMSR-E [*Kawanishi et al.*, 2003] are incorporated to achieve a realistic representation of microwave sensor-observable Tb [*Matsui*, 2013].

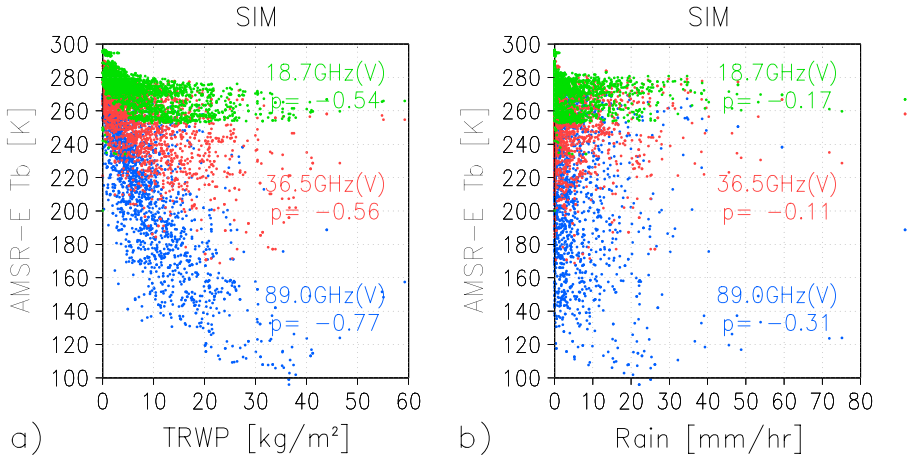

Figure 5. Scatterplots of AMSR-E Tb and (a) total rain water path (TRWP) and (b) surface rainfall rate. Pearson correlation coefficients are also shown in the plot.

Figure 4b shows AMSR-E $Tb_{89GHz(V)}$ simulated from the NU-WRF simulation. Similar to the observation, the simulated MCS generates a region of $Tb_{89GHz(V)}$ low Tb in the middle of the domain, which is associated with cold-rain processes. Figure 4c shows the geolocation error of raining pixels. A region of $Tb_{89GHz(V)}$ depression is shifted ~400 km between the observation and the simulation, suggesting the forecast errors. This spatial analysis of microwave Tb can be further used for microwave radiance-based precipitation assimilation [*Aonashi and Eito*, 2011; *Zupanski et al*., 2011a; *Zhang et al*., 2013]. Figure 4d shows the cumulative frequencies for 89 GHz, 36.5 GHz, and 18.7 GHz channels sampled only from the scattering pixels of $Tb_{89GHz(V)}$ less than 270 K (i.e., raining pixels in Figure 4b). Compared to the observations, the simulation overestimates the depression of Tb for all frequencies, especially at 89 GHz, suggesting the overestimation of ice aloft and the uncertainties due to size and effective density [*Matsui et al*., 2009; *Han et al*., 2013] or alternatively uncertainties of ice single-scattering properties [*Meirold-Mautner et al*., 2007]. However, we should mention that Mie calculation with effective mixture assumption, implemented in this study, tends to have larger forward scattering than realistic nonspherical models; thus, Tb depression become even larger with more realistic nonspherical snow single-scattering model [*Liu*, 2004].

We should emphasize that the purpose of using microwave Tb to analyze precipitation processes and microphysics over land, instead of using surface precipitation product, is to avoid the large uncertainties of precipitation estimates from satellite passive microwave sensors. One uncertainty of microwave-based rainfall estimates is attributed to the complex profile of raining and nonraining particles. Unlike radar, a passive microwave imager receives microwave emission/scattering signals from the entire atmospheric profiles and surface. Thus, microwave signals are more directly linked to the column total rainwater path (TRWP) than surface rainfall rate [*Liu and Curry*, 1992].

Figure 5 demonstrates (a) the correlations of TRWP and AMSR-E Tbs and (b) the correlations of surface instantaneous rainfall rate and AMSR-E Tbs from the NU-WRF simulation. It is obvious that the microwave Tb depressions are better correlated with total rainwater path (Figure 5a: $p = -0.77$ at 89 GHz, $p = -0.54$ at 36.5 GHz, $p = -0.54$ at 18.7 GHz) than the surface rainfall rate (Figure 5b: −0.31 at 89 GHz, −0.11 at 36.5 GHz, −0.17 at 18.7 GHz). High-frequency $Tb_{89GHz(V)}$ is depressed more than the low-frequency Tb in response to TRWP due to its shorter wavelength and the smaller footprint size.

Surface rainfall rate, in this context, is the instantaneous rainfall flux at the surface, which is more closely related to "near-surface" liquid rain rather than the ice aloft. Low-altitude liquid raindrops can be detected from the low-frequency emission only if surface emissivity is sufficiently small, such as over water bodies (lake and ocean). However, land surfaces typically have high surface emissivity that obscures the emission signal from near-surface rain. Therefore, rainfall retrieval over land heavily relies on high-frequency Tb depressions associated with ice aloft [*Kummerow et al*., 2001]. Continental dry boundary layers often evaporate raindrops before reaching the surface, i.e., virga [*Fraser and Bohren*, 1992]. All of these issues hamper rainfall retrieval over land. Thus, for given uncertainties in the over-land rainfall retrieval by passive

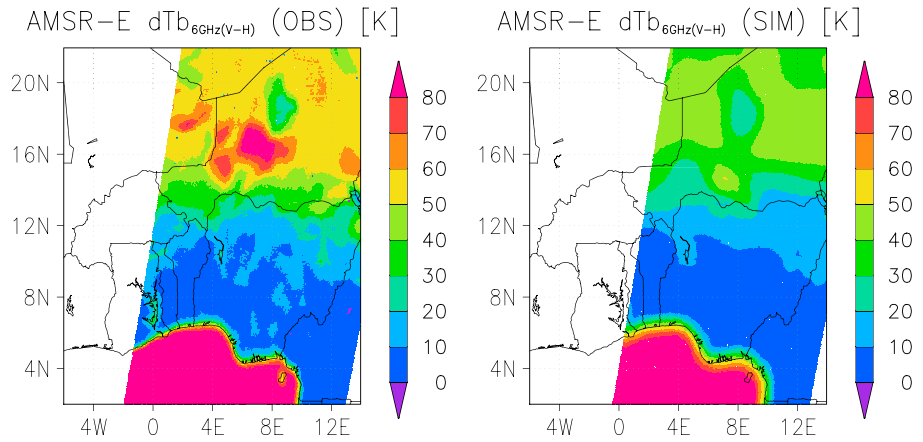

Figure 6. Polarization difference (Tb(V) − Tb(H)) in AMSR-E Tb at 6 GHz from the observation (OBS) and simulation (SIM). Observation shows very strong polarization difference under the area of the MCS, indicating the presence of standing water.

microwave remote sensing, it is more direct to compare microwave Tb depression between satellite observations and model simulations than surface rain rate, as long as microwave Tb is properly simulated from the model.

Over land, at low microwave frequency such as 6 GHz, the atmosphere becomes more transparent, and the signals of cloud and precipitation particles become negligibly small. At this frequency, TOA microwave radiance is most sensitive to the surface conditions: water/land surface, wetness, soil-vegetation roughness, and terrain structure. AMSR-E has been used for retrieving the land surface soil moisture [*Njoku et al.*, 2003] and flood detection [*Temimi et al.*, 2012]. The emissivity-polarization difference (difference of Tb between vertical and horizontal polarization) of low-frequency microwave Tb is very sensitive to the presence of surface standing water [*Prigent et al.*, 2007]. Figure 6 shows the polarization difference of microwave brightness temperature (dTb_{6GHz} = Tb(V) − Tb(H)) from AMSR-E Tb at 6 GHz. Over ocean, dTb_{6GHz} ranges up to 80 K due to large emissivity-polarization difference of water bodies. The simulation from NU-WRF shows the same large values of dTb_{6GHz} over the ocean. However, AMSR-E observations also show the large depression of dTb_{6GHz} around the area of MCS area over land, while there is no such large dTb_{6GHz} in the simulation. Note that MODIS $Tb_{11\mu m}$ and AMSR-E Tb_{89GHz} demonstrated that MCSs are in both the observed and simulated scene (Figures 1 and 4).

Although there are no in situ observations, the ocean-equivalent level of the dTb depression over land suggests the presence of significant amount of standing water due to temporary flooding from the propagating MCSs [*Prigent et al.*, 2007; *Temimi et al.*, 2012]. Flooded grassland and savanna (around the Sahara-Sahel border) are very common in the tropics and subtropics area over this region. The standing water greatly changes the surface emissivity from land (~0.9) to water (~0.4), and as a result, TOA polarization differences become very large and close to that of ocean. The missing Tb depression in Figure 6b is a direct result of (i) no parameterization of this effect in the model and (ii) using the empirical land surface emissivity database TELSEM, which is a monthly scale climatology that does not account for intramonth or interannual surface water variability. TELSEM has been developed mainly to provide first-guess emissivity information that is refined during a retrieval process (e.g., assimilation) although the direct use of TELSEM, as in this study, for simulation/observation comparison has shown its positive impact in most continental areas [*Aires et al.*, 2011].

To improve forward calculations, the inundated area must be treated as water body for computing the surface emissivity. Unfortunately, the Noah Land Surface Model (LSM) used in the NU-WRF simulation does not predict standing water; rather, all residuals of surface rainfall, canopy interception, and surface infiltration become runoff to discharge into rivers immediately without surface ponding. Surface-standing water is an important (and ongoing in land component in the NU-WRF) consideration for future LSM development within the Earth System modeling system [*Dadson et al.*, 2010], not only for improved surface emissivity and forward radiative transfer modeling but also for better describing surface energy exchanges and skin temperatures.

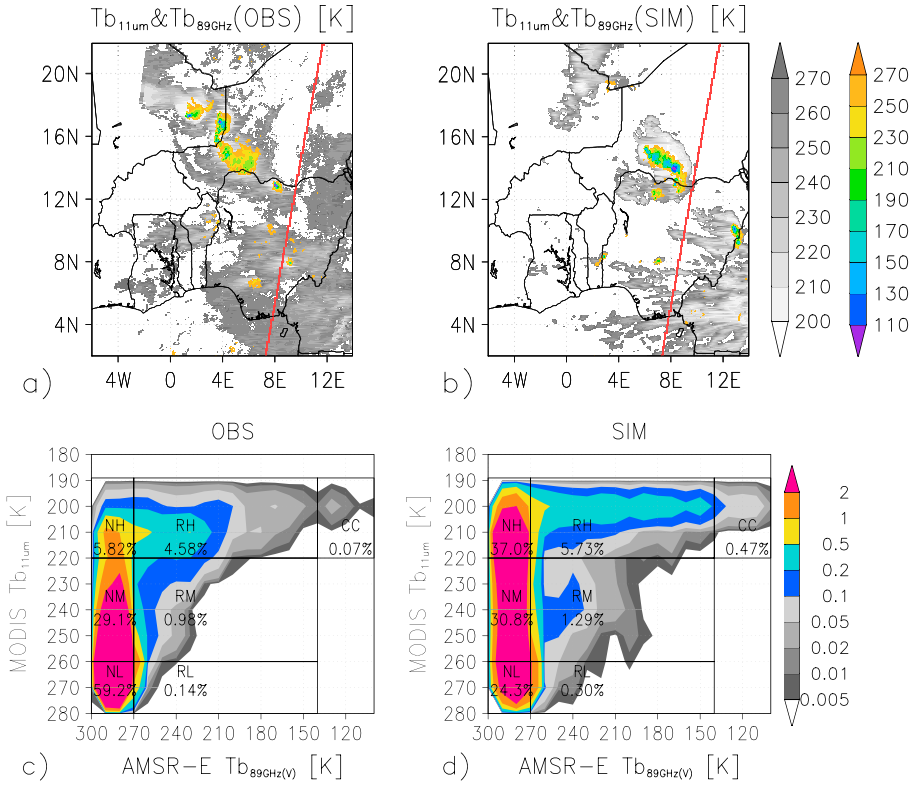

Figure 7. (a) Observed and (b) simulated combined AMSR-E $Tb_{89GHz(V)}$ and MODIS $Tb_{11\mu m}$ for the period corresponding to Figure 4. MODIS $Tb_{11\mu m}$ is shown only if Tb is less than 273 K (gray shade), and AMSR-E $Tb_{89GHz(V)}$ is shown only if Tb is less than 270 K (color shade). Red line is CALIPSO-CloudSat overpass. (c) Observed and (d) simulated joint MODIS $Tb_{11\mu m}$-AMSR-E $Tb_{89GHz(V)}$ histogram (color bars represent frequency in %). Clouds are categorized into seven classes based on artificial thresholds of MODIS $Tb_{11\mu m}$ and AMSR-E $Tb_{89GHz(V)}$: Nonraining low cloud (NL), nonraining middle cloud (NM), nonraining high cloud (NH), raining low cloud (RL), raining middle cloud (RM), raining high cloud (RH), deep convective core (CC). Populations of each category are also displayed.

4.3. Combined Aqua Microwave-Infrared Brightness Temperature

One primary benefit of using simultaneous multisensor satellite observations and simulators is to take advantage of the different signal sensitivities (e.g., AMSR-E 89 GHz and MODIS 11 μm IR channels). The previous sections show the $Tb_{11\mu m}$ sensitivity to the T_{CT} and microwave Tb sensitivity to ice aloft. If these are combined, it allows a more complete view of cloud-precipitation processes [*Liu et al.*, 1995]. Figures 7a and 7b shows the MODIS $Tb_{11\mu m}$ (below 273 K, gray shade) overlaid with the AMSR-E $Tb_{89GHz(V)}$ (below 270 K, color shade). The picture clearly shows the AMSR-E Tb depressions (raining pixels) are located in the middle of the gray-shaded convective system. In the south part of the domain, the combined observations show the presence of midlevel clouds under cold-rain processes; these are also seen in the simulation, although geolocations are quite different.

For a more quantitative analysis in the domain, joint diagrams of the MODIS $Tb_{11\mu m}$ and the AMSR-E $Tb_{89GHz(V)}$ are formed (Figures 7c and 7d). This is a combination of histograms from Figures 1d and 4d but provides an additional dimension in occurrences of different cloud types. Our joint diagram is very close to that of *Liu et al.* [1995], which uses IR Tb and *microwave index* that accounts for both scattering and emission of microwave Tb, since their focus region was over ocean, where emission signals could be detected. This method is to simply use depression (scattering signals) of high-frequency microwave Tb in addition to IR Tb, thereby allowing validation over land.

Two thresholds in the $Tb_{11\mu m}$ are selected; a 220 K threshold for separating high and middle clouds, while a 260 K threshold for separating middle and low clouds [*Matsui et al.*, 2007]. Often used is 220 K as a threshold of rainfall pixels, such as for the GOES precipitation index [*Arkin et al.*, 1994]. We also use two

thresholds for $Tb_{89GHz(V)}$: 270 K for separating raining and nonraining clouds, and 130 K for identifying very large amounts of ice, associated with deep convective cores [*Olson et al*., 2001b]. With these selected thresholds, we can group the observed microwave IR Tb into seven categories of cloud levels and precipitation (Figure 7c): Nonraining low cloud (NL), nonraining middle cloud (NM), raining low cloud (RL), raining middle cloud (RM), raining high cloud (RH), and deep convective core (CC).

These classifications, thresholds, and interpretations could and should vary depending on the environment: e.g., maritime, midlatitude or high-latitude have different types of cloud-precipitation processes, background temperatures, and humidity profiles, since the exact link between the "rainfall rate" and $Tb_{89GHz(V)}$ depression is difficult to identify with passive microwave imagers (Figure 5). We should also mention that IR Tb range of $Tb_{11\mu m}$ between 220 and 260 K cannot be attributed to midlevel clouds only as discussed before. It is well known that cirrus and midlevel clouds can have the same brightness temperature in the infrared window [*Chaboureau and Pinty*, 2006].

The overarching point here is that this categorization can be made from the satellite-measured L1 radiance data without any physical assumption of a satellite retrieval algorithm, and the same diagram can be made from the simulation through the multiinstrumental simulators. Figure 7d shows the simulated joint $Tb_{11\mu m}$-$Tb_{89GHz(V)}$ diagram from the NU-WRF simulation. In general, the simulation captures qualitatively similar distributions to the observed diagram but with quantitative differences (Figure 7c). Satellite observations suggest that total nonraining cloud classes (NL + NM + NH) occupy 94.6% of total pixels, while the simulation diagram shows 91.6% of all pixels, which are quite similar. However, among nonraining classes, high clouds (NH) are 5.6% (=5.33%/94.6%) in the observed diagram and 36.6% (=33.5%/91.6%) in the simulation, while low clouds (NL) are 66.2% (=62.6%/94.6%) in the observed diagram and 32.3% (=29.6%/91.6%) in the simulated diagram. Thus, the simulation severely overestimates nonraining high clouds (NH) and underestimates nonraining low clouds (NH).

Further among high raining pixels (RH + CC), one can estimate the convective-stratiform ratio, 1.3:98.7 in the observations and 2.0:98.0 in the simulations, which are quite close to each other. This is a practical and consistent way to separate convective and stratiform rain fraction for both observation and simulation, since most of the traditional methods are either simulation-based (using updraft velocity) or observation-based (using melting layer) methods [*Lang et al*., 2003].

Alternative cloud classifications have been proposed before: (i) the International Satellite Cloud Climatology Project (ISCCP) cloud diagram that classifies cloud type by cloud top pressure and optical depth via visible IR sensors [*Rossow and Schiffer*, 1991] and (ii) a H_{et}-Tb_{IR} diagram that classifies raining cloud type via radar echo top height and IR Tb [*Masunaga et al*., 2008; *Matsui et al*., 2009]. One advantage of this joint MODIS $Tb_{11\mu m}$-AMSR-E $Tb_{89GHz(V)}$ over the ISCCP classification [*Rossow and Schiffer*, 1991] is that observations are always available at both daytime and nighttime pass, since this does not rely on visible channels. Alternatively, one advantage of the ISCCP classification over the MODIS $Tb_{11\mu m}$-AMSR-E Tb_{89GHz} diagram is that cirrus is well determined, because of using visible band (identifying cloud optical depths). Another advantage of this method over the H_{et}-Tb_{IR} classification [*Masunaga et al*., 2008] is that passive IR and microwave sensors have large spatial coverage (1445 km of swath: AMSR-E) in comparison with radar instruments (250 km of swath). In addition, similar diagrams can be constructed from various satellites that carry passive visible IR and microwave sensors, such as the Tropical Rainfall Measurement Mission and Suomi National Polar-orbiting Operational Environmental Satellite System Preparatory Project satellites, to name a few.

4.4. CALIPSO, CALIOP, and CloudSat CPR Sensors

Space-borne active sensors are relatively new instruments in comparison with passive instruments. Active sensors transmit electromagnetic energy to Earth, and backscattered energy is used to determine the distance and characteristics in the atmosphere and surface. Simultaneous use of active- and passive-sensor observation also avoids nonsingularity issue of single-channel radiance-based evaluation approach as mentioned in section 2. The Cloud-Aerosol Lidar with Orthogonal Polarization (CALIOP) is a dual-wavelength (562 nm and 1064 nm) polarization-filtered lidar aboard the Cloud-Aerosol Lidar and Infrared Pathfinder Satellite Observations (CALIPSO) satellite [*Winker et al*., 2009]. The CALIPSO satellite is part of the A-Train Constellation and has provided on-nadir view of vertical profiles in clouds and aerosols since April 2006

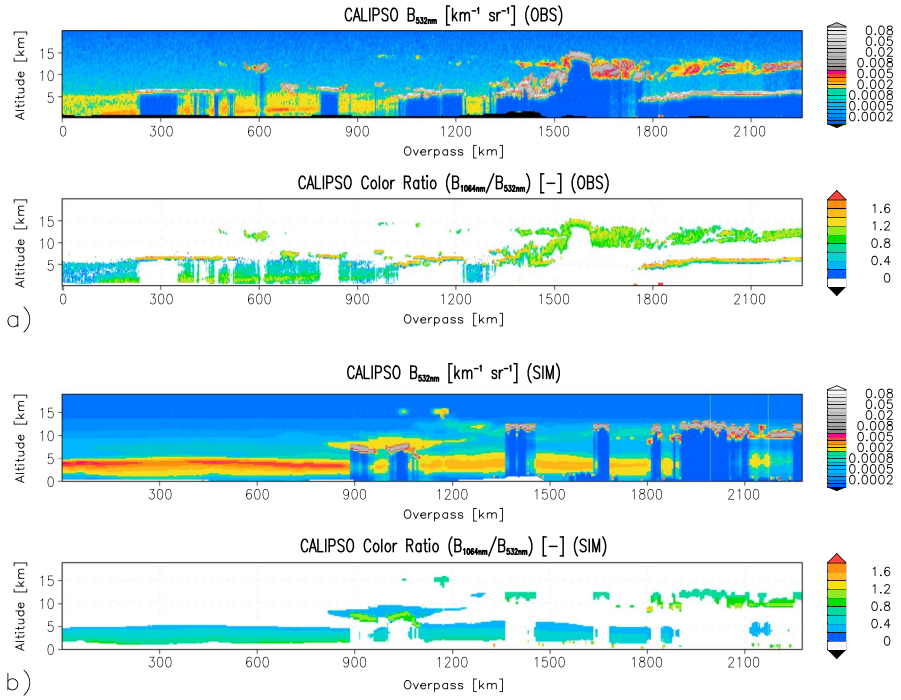

Figure 8. (a) Observed and (b) G-SDSU simulated CALIPSO CALIOP B_{532nm} ($km^{-}1\ sr^{-1}$) and color ratio (B_{1064nm}/B_{532nm}) over the West Africa. CALIPSO satellite overpassing is shown in Figures 7a and 7b. Overpassing of 0 –2200 km corresponds to north-to-south orientation.

[*Winker et al*., 2007], complemented by the wide-view images from the AMSR-E and the MODIS instruments of the Aqua satellite. Lidar backscattering signals have been simulated for assessing ice clouds [e.g., *Chiriacho et al*. 2006] and mineral dust [e.g., *Chaboureau et al*., 2011].

Figure 8a shows CALIPSO backscatter signals B_{532nm} and color ratio ($R_{532nm/1064nm} = B_{532nm} / B_{1064nm}$) over West Africa (where CALIPSO overpass information is shown in Figure 7). Small backscatter (B_{532nm} less than 0.001 $km^{-1}\ sr^{-1}$, blue shade) represents atmospheric molecular densities; medium backscatter (B_{532nm}: 0.001–0.05 $km^{-1}\ sr^{-1}$, yellow-to-red shade) represents either mineral dust particles (color ratio less than ~1.2) over the Saharan desert below 5 km above sea level (ASL) or ice crystals (color ratio greater than ~1.2) of cirrus clouds above 10 km ASL; and strong backscatters (B_{532nm} greater than 0.05, white shade) suggest presence of liquid cloud droplets from the boundary layer clouds across the domain. In general, cloud liquid droplets have much larger extinction than ice crystals and mineral dust particles [*Yoshida et al*., 2010; *Zhang et al*., 2010; *Hu*, 2007]. Backscatter signals below thick ice clouds or liquid clouds are strongly attenuated due to large extinction by cloud layers. As discussed in analysis of the previous section, high MODIS $Tb_{11\mu m}$ (~273 K, dark patchy shade in Figure 8a) represents shallow clouds capping a deep continental boundary layer at ~5 km ASL. Medium ranges of the MODIS $Tb_{11\mu m}$ (~220 K, gray shade in Figure 7a) in the south of the domain are revealed as shallow boundary layer clouds overlapped by cirrus clouds, which could not be revealed by diagnosing $Tb_{11\mu m}$ only, although two-channel IR Tb techniques permit validating cirrus clouds [*Chaboureau and Pinty*, 2006].

The G-SDSU lidar simulator is built upon the identical visible IR optics module that shares single-scattering parameters between visible IR simulator and lidar simulator. The lidar simulator utilizes total extinction and backscattering (phase function of 180°) for computing the total backscattering coefficient at wavelength of λ (β_λ),

$$\beta_\lambda = \sigma_\lambda(l)\exp\left[-2\int_0^l \tau_\lambda(l)\mathrm{d}l\right],$$

where σ_λ is a total backscattering coefficient that integrates molecular, aerosol, and cloud backscattering coefficients; and τ_λ is total optical depth that also integrates molecular, aerosol, and cloud optical depths

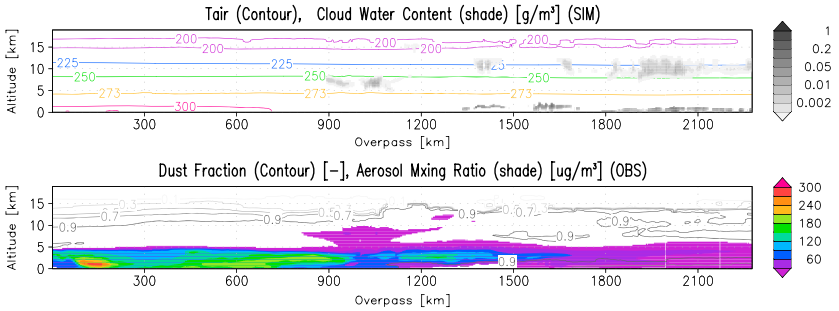

Figure 9. (top) Temperature and cloud (ice and liquid) water content resampled along the CALIPSO overpass. (bottom) Dust fraction (contour) and total aerosol mass concentration (shaded) from the NU-WRF simulation along the CALIPSO lidar simulation. CALIPSO satellite overpassing is shown in Figures 7a and 7b. Overpassing of 0–2200 km corresponds to north-to-south orientation.

[*Platt*, 1973]. The exponential term represents attenuation of lidar signals from instrument to the target atmosphere, represented by the length, *l*. Multiple scattering and instrumental random noise are not included in the lidar module [*Hogan and Battaglia*, 2008], since the model evaluation does not focus on microphysics profiles in the thick clouds using the CALIOP instruments.

Figure 8b shows the simulated CALIOP backscatter signals B_{532nm} and color ratio over West Africa. The simulated CALIOP signals show realistic B_{532nm} profiles that represent background molecular density, aerosols, and cloud profiles. Aerosol signals are distributed around up to 5 km ASL over the Saharan desert, while cirrus cloud signals are distributed around 10–15 km ASL over the ocean. These are in reasonable agreement with the observations (Figure 8a). However, as pointed out in the $Tb_{11\mu m}$ analysis, shallow boundary layer clouds are missing in the NU-WRF simulations in the domain. Also, dust signals appear to be too strong in NU-WRF, and simulated B_{532nm} begins attenuation in the middle of the dust layer.

Figure 9 shows the NU-WRF-simulated geophysical parameters along the CALIPSO overpass. Temperature profiles indicate the freezing level is near 4 km above ground level (AGL). Liquid cloud droplets are present below 2 km ASL. Aerosol mass concentration is mostly confined below 5 km ASL, and mineral dust represents more than 90% of total aerosol mixing ratio in this level. Between 900 and 1200 km of the horizontal transect, mineral dust overshoots to 5 km ASL, and it creates unrealistic CALIPSO dust signals in the middle troposphere. Thus, as pointed out earlier, the NU-WRF simulation overestimates the amount of mineral dust, and the simulated backscatter signals are strongly attenuated near the surface.

The CloudSat Cloud Profiling Radar (CPR) is the first spaceborne 94 GHz (W band) cloud radar [*Tanelli et al.*, 2008]. This millimeter wavelength radar resolves cloud and light precipitation processes along with the nearly simultaneous CALIPSO measurements and also overlaps with other A-Train satellite measurements [*Stephens et al.*, 2002]. Figure 10 shows observed and simulated CloudSat CPR radar reflectivity profile (color shade) on the background of the CALIPSO B_{532nm} signals (gray shade). This clearly demonstrates the different capabilities of lidar and cloud radar instruments. For example, most of the thin boundary layer-

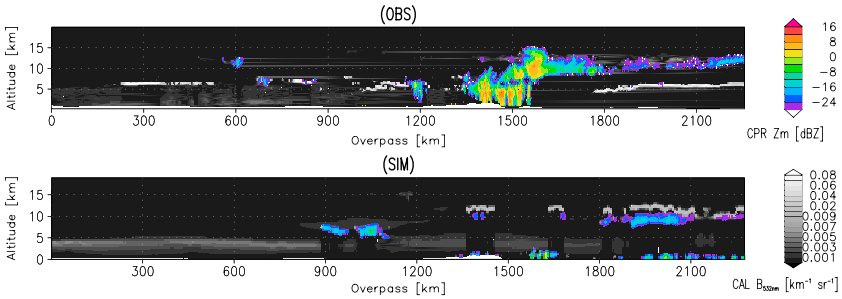

Figure 10. (top) Observed and (bottom) simulated CloudSat CPR reflectivity (color shade) along with the CALIPSO CALIOP backscattering signals (gray shade). CloudSat satellite overpassing is shown in Figures 7a and 7b. Overpassing of 0–2200 km corresponds to north-to-south orientation.

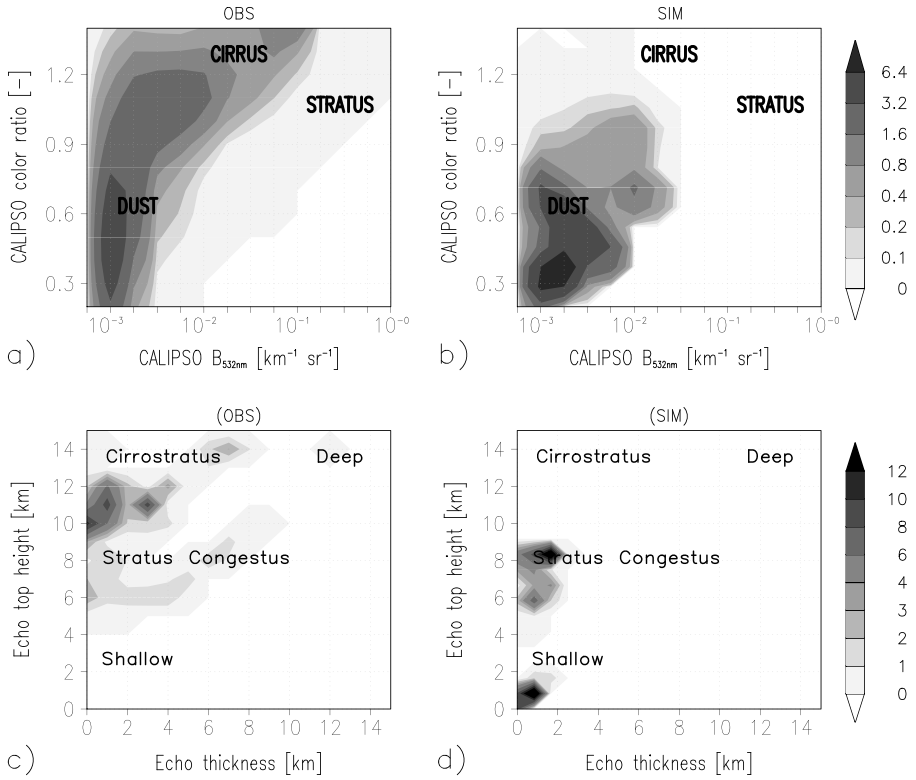

Figure 11. Statistical composites of (a) observed and (b) simulated CALIPSO CALIOP joint B_{532nm}-$R_{532nm/1064nm}$ diagrams. Statistical composite of (c) observed and (d) simulated CloudSat CPR joint H_{echo}-H_{top} diagram. These diagrams suggest statistical populations of different aerosol and cloud types (gray bars represent frequency in %).

capped clouds and mineral dust layers are undetected by CloudSat, while the CloudSat radar reflectivity (Zm) profile reveal the vertical extent of the deep convection and associated anvil. Simulations show similar features of CPR signals below the CALIOP attenuation in the cloudy columns, while NU-WRF misses the convection in the middle of the domain due to the forecasting error, resulting in the missing CPR signals. The NU-WRF simulation also shows some dense-fog signals very low to the surface (below 2 km AGL) across the right portion of the overpass, probably because of using fixed sea surface temperature, although this near-surface fog cannot be evaluated by the CloudSat observations due to surface clutter impact.

For more quantitative analysis, these vertical profile data can be recast in various statistical formats. Figure 11a shows the CALIOP joint B_{532nm}-$R_{532nm/1064nm}$ histogram (probability density). This diagram has been used for the CALIPSO operational algorithm to classify backscattering signals into different aerosols and cloud types [*Omar et al*., 2009]. For example, dust signals generally have lower backscatter (less than 0.005) and moderate color ratio (0.2–0.8). Cirrus clouds tend to have larger color ratio (greater than 0.8) and moderate backscatter (less than 0.1). Middle and low stratus have liquid cloud droplets that peak strong backscatter (greater than 0.1) and higher color ratio (greater than 0.9).

In contrast, the simulated values show a much different distribution across the joint B_{532nm}-$R_{532nm/1064nm}$ diagram. Overall, the color ratio tends to be small, and backscatters are also ranged below 0.1 due to lack of the boundary layer clouds in the NU-WRF simulation. Dust backscatter is too large due to overestimated dust amount in NU-WRF. Although cirrus clouds are abundant over the ocean in the NU-WRF simulation, both the simulated backscatter and color ratio signals are too weak. These statistical biases suggest the presence of cloud-aerosol microphysics biases in this NU-WRF simulation (e.g., PSDs) or in the G-SDSU's assumption of single scattering (Lorenz-Mie). Usually, spherical assumption create strong backscattering peak in comparison with nonspherical solutions.

Figure 11b shows CloudSat CPR joint diagrams, which mimic the ISCCP diagram that use cloud top pressure and cloud optical thickness. The current diagram, instead, utilizes the CPR echo top height (H_{top}: from-TOA-

to-BOA first pixels with three-consecutive significant (>-28 dBZ) Z_m signals) and echo thickness (H_{echo}: depth of continuous significant Z_m signals). The observed diagram shows a spectrum of cloud types: the small fraction of deep clouds and large fraction of midlevel clouds as shown in the horizontal strip (Figure 10). On the other hand, the simulated H_{echo}-H_{top} diagram captures the stratus and near-surface clouds only. These are visibly comparable to the horizontal strip in Figure 10, but the statistical plots can more quantitatively assess the amounts of different cloud types.

While the combination of the CloudSat and the CALIPSO measurements successfully infers the vertical profile of the atmosphere [*Mace et al*., 2009; *Stein et al*., 2011], these two instruments are nadir-viewing sensors; thus, the spatial coverage is extremely limited in comparison with the passive visible IR or microwave sensors as discussed in the previous sections. Examples of the statistical composite (especially CloudSat) in our example are mostly attributed to forecasting errors. Therefore, CloudSat-CALIPSO data should be analyzed through ensemble, long-term, or large-scale sampling for representing robust statistics, or must be used in combination with wide-viewing passive sensors in the case of evaluating short-term model simulations.

Both the CALIPSO B_{532nm} and the CloudSat CPR Z_m can be further formed into a contoured frequency of altitude diagram (not shown here) to evaluate cloud and aerosol microphysics. More comprehensive cloud microphysics evaluation using the CALIPSO/CloudSat backscattering measurements has been explored in *Hashino et al*. [2013]. Several cautions are discussed here for cloud-aerosol microphysics analysis using the CloudSat CPR and the CALIPSO CALIOP backscattering measurements.

First, multiple scattering must be well represented in the forward model (not performed in this paper), if one aims to diagnose CALIPSO backscatter within any kind of clouds or CloudSat Zm within deep convective clouds [*Winker*, 2003; *Hogan and Battaglia*, 2008]. If not treated, multiple-scattered signals (pixel) must be discarded from the analysis, using threshold of Zm [*Battaglia et al*., 2008; *Hashino et al*., 2013].

Second, uncertainties of single-scattering properties for simulating active instruments often become as large as uncertainties from the particle composition and sizes when single scattering regimes of targeting particles depart from Rayleigh scattering regime. For example, ice crystals and aggregate for CloudSat CPR (W band) and mineral dust and ice crystals for CALIPSO CALIOP sensor (564 nm). More discussion is explored in recent studies [*Liu*, 2004; *Petty and Huang*, 2010; *Baum et al*., 2005]. The bottom line is that the nonspherical shape greatly affects backscattering signals and variability of phase functions and more realistic computations from the T-matrix method [*Mishchenko et al*., 2004] or discrete dipole approximation (discrete dipole scattering) [*Draine and Flatau*, 1994] tend to reduce backscattering efficiency by smoothing the variability of phase function, if particles are randomly oriented. On the other hand, total extinction and single-scattering albedo or asymmetry parameter are relatively less affected, since these parameters are integrated over the entire scattering angles.

Third, particle size distributions (PSDs) of aerosol and cloud microphysics are preferably prognostic parameters (two- or higher-order moments). If these are diagnostic parameters, there is little physical reasoning to conduct detailed evaluation, unless the diagnostic microphysics parameters are consistently represented and functioning in other physics processes, such as radiative heating (diagnostic PSDs affect broadband single-scattering properties), terminal velocity (PSDs changes sedimentation of hydrometeor or dry depositions of aerosols), and other microphysics processes (collision coalescence processes of hydrometeor, coagulation of aerosols, etc.).

5. Summary and Conclusion

Through reviewing different types of analyses, multisensor satellite radiance-based evaluation methods clarify the strengths and weaknesses of the NU-WRF simulation over West Africa. The spatial differences reveal forecast errors, while the statistical composites tend to reveal biases in physics modules in the NU-WRF simulation. Although this limited results cannot generalize the conclusion for NU-WRF performance of different environments, these physics biases are summarized as follows:

Cloud Microphysics: Both IR Tb and CALIPSO backscatter evaluation revealed that the NU-WRF underpredicts boundary layer shallow clouds, while IR and microwave Tb evaluation suggested that NU-WRF overestimates cold-rain processes. These biases critically affect regional energy-radiation budget biases.

Land surface: Time series analysis of IR Tb from Meteosat suggested that the amplitude of diurnal cycles in daytime skin temperature is underestimated in the NU-WRF simulation over cloudless pixels. Polarization differences in low-frequency microwave Tb suggest the presence of flooded grassland and savanna. The current version of the Noah LSM and empirical emissivity databases do not predict such processes and polarization-emissivity differences, and they must be accounted for to better represent surface energy fluxes over the subtropical savanna regions.
Aerosols: Strong backscatter and attenuation of the CALIPSO backscatter suggests that mineral dust aerosols are overestimated in the NU-WRF simulation. The dust overestimation is due to the initial attempt of adapting the GOCART scheme on the cloud-resolving-scale simulations. The Goddard Chemistry Aerosol Radiation and Transport (GOCART) has been developed and applied for climate-scale modeling (horizontal grid spacing is about 1–2°). On this storm-resolving-scale simulation, surface winds become sharper by explicit treatment of mesoscale dynamics; thus, it tends to overestimate surface dust emission using default wind threshold values.

Within the coupled modeling system, biases of physics modules summarized in this section are interactive among different physics modules. For example, if dust emission is suppressed with improved surface process, it alters atmospheric radiative heating rates (both shortwave and longwave) and could suppress ice nuclei concentrations and, consequently, ice crystal production, which could modulate microphysics and macrophysics structure of clouds precipitation processes. Changes in radiative heating can change local thermodynamic profiles and mesoscale circulations and the timing of deep convection. Improvement of microphysics could significantly adjust surface and atmospheric energy balance, alter surface precipitation rates, and change soil moisture amount. Modification of the land surface parameterization also impacts atmospheric processes and alters feedbacks with microphysics and aerosol processes.

Therefore, for a fully coupled regional Earth System model, multisensor evaluation methods, demonstrated in this manuscript, are encouraged to investigate overall performance and improvement, while avoiding local tuning with use of limited satellite products or the limited number of radiance observations. Needless to say, multievent, multiseason simulations, and ensemble forecasting over various climate regimes will provide more robust evaluation of model dynamics and physics performance.

As summarized in section 2, radiance-based evaluation relies on understanding the radiance and backscatter characteristics at different wavelengths and from different sensor platforms. Satellite raw radiance contains more geophysical information from many atmospheric and land surface sources simultaneously. It often provides benefit for evaluating various aspect of Earth System modeling. Users may create a customized algorithm based on thresholds or simple statistical processes, as shown in our manuscript, to focus on a specific geophysical parameter (either clouds, aerosols, or land) for evaluation. Readers may be interested in other studies using similar approaches and alternative approaches through a number of references cited in this manuscript.

The methods discussed in this manuscript can be applied to any regional model using multisensor satellite measurements currently present in the space. Multiinstrumental radiance-based evaluation methods have been initiated in recent years, coinciding with emergence of new satellite measurements, and there are a number of different ways to interpret satellite radiance data and novel techniques to evaluate models. This type of evaluation activity for regional Earth System modeling has been often lacking before. Therefore, the principal aim of this manuscript is, by addressing simple examples, to motivate the modeling community to properly and creatively incorporate the wealth of satellite measurements and instrumental simulators when employing complex regional Earth System modeling analysis and development practices.

Appendix A: Single-Scattering Properties

NU-WRF's native output can be directly processed by the G-SDSU. At each grid cell, NU-WRF output provides (i) vertical profiles (terrain following coordinate) of temperature, geopotential height, pressure, humidity, hydrometeors, and aerosols; and (ii) also provides surface fields including surface skin temperature, surface pressure, terrain elevation, surface types, and latitude and longitude coordinates, which necessarily characterize surface boundary conditions of radiative transfer. Information on hydrometeors and aerosols depends on the complexity of the parameterizations used by the model. In addition to the Goddard microphysics scheme, the G-SDSU supports the Lin scheme [*Lin et al.*, 1983], WRF single-moment six-class

microphysics scheme [*Hong and Lim*, 2006], National Center for Atmospheric Research two-moment scheme [*Morrison et al*., 2005], Regional Atmospheric Modeling System one and two-moment schemes [*Walko et al*., 1995; *Meyers et al*., 1997], and Hebrew University Cloud Model Spectra Bin Microphysics [*Khain et al*., 2005]. For aerosols, the G-SDSU currently supports the GOCART scheme.

The consistency with model physics and different satellite simulators is a very important feature of the G-SDSU, allowing physically consistent treatment between simulated geophysical parameters and single-scattering integration (described later) among different satellite simulators. More details are explained hereafter.

For hydrometeors, the Goddard bulk one-moment microphysics scheme [*Lang et al*., 2007, 2011] explicitly predicts mass mixing ratio for cloud droplets (q_c), rain drops (q_r), ice crystals (q_i), snow aggregates (q_s), and graupel (q_g). PSDs for rain, snow, and graupel are assumed to obey the following function:

$$\mathrm{d}N(D) = N_o D^{\mu} \exp(-\lambda D)\, \mathrm{d}D,$$

where N is the particle number concentration, D is a particle diameter, N_o is an intercept parameter, μ is a shape parameter, and λ is a slope parameter. For rain, snow, and graupel particles, μ is set to be zero (e.g., exponential size distribution). The total particle number concentration (N_t) is now expressed as

$$N_t = \int N(D) dD,$$

and mass is expressed by integration of number concentrations and unit-particle mass,

$$q = \frac{\pi}{6} \int D^3 \rho(D) N(D) \mathrm{d}D$$

where ρ is particle density. For the one-moment scheme, N_o is assumed to be constant for rain and graupel, and λ (inverse of effective particle size) varies as a function of total mass (q). This means that larger mixing ratios have larger mean particle size. For snow, λ and N_o are parameterized by temperature and total mass to mimic aggregation growth [*Lang et al*., 2011]. Cloud liquid particles applies the generalized gamma size distributions with fixed effective radius (9 μm in this study). Cloud ice crystal applies a temperature-dependent effective radius following the empirical fitting from aircraft measurements [*Heymsfield and Platt*, 1984]. These specifications are consistent to the microphysics and radiation scheme in the NU-WRF.

The GOCART scheme predicts mass mixing ratio of dust (q_{dust}), sulfate (q_{so4}) and its precursor SO_2 (q_{so2}), black carbon (q_{bc}), and organic carbon (q_{oc}), sea salt (q_{ss}), and other gaseous species. The PSD function is assumed to be a lognormal distribution of radius (r).

$$\mathrm{d}N(r) = \frac{N_t}{\sqrt{2\pi} r \log\sigma \ln 10} \exp\left[\frac{1}{2}\left(\frac{\log r - \log r_{\mathrm{mod}}}{\log\sigma}\right)\right] \mathrm{d}r$$

where σ is standard deviation, r_{mod} is mode radius, and N_t is the total number concentration. Dust and sea salt have multimode PSDs, and each mode of mixing ratio is explicitly simulated [*Chin et al*., 2000; *Ginoux et al*., 2001]. More importantly, the radius and PSDs of hygroscopic species (sulfate and its precursor, organic carbon, and sea salt) depend largely on relative humidity. Refractive index and mode radius of each species are essentially based on the optical properties of aerosols and clouds (OPAC) database [*Hess et al*., 1998].

The G-SDSU converts this particle information (sizes and species) to single-scattering properties, including extinction efficiency, single scattering albedo, moments of phase function, and backscattering coefficients. By default, the G-SDSU computes single-scattering properties through the Lorenz-Mie solution with an a priori database of the complex refractive index. Since the Mie calculation is the exact analytical solution of the Maxwell's theory for a perfect spherical particle, it simply requires inputs of size parameter ($X = \pi D/\lambda$) and refractive index database.

Microwave complex refractive indices of hydrometeors (e.g., water and pure ice) are derived through laboratory experiments, and their value depends mostly on wavelength and slightly on temperature [*Hufford*, 1991]. For solid particle in the microwave ranges, if the size parameter is reasonably small ($X \sim 2$: Rayleigh regime, typically at low-frequency microwave spectrum), one can apply effective mixture solution (i.e., a fluffy sphere approximation) for effective refractive index of mixture of ice and air [*Bohren and Battan*, 1980]. There are two approximations available in the G-SDSU: (i) the Maxwell-Garnet approximation that assumes ice (air) matrix and oblique air (ice) inclusion and (ii) the effective medium approximation that assume homogeneous mixing of ice and air [*Bohren and Battan*, 1980]. These approximations can be further applied

to the mixed-phase (melting) particles and result in quite different magnitudes for simulating the melting band in radar reflectivity [*Olson et al*., 2001a]. The effective mixture approximation is inaccurate, when the size parameter becomes larger than ~2 and more. In this case, a more sophisticated single-scattering model is required in order to treat nonspherical particle shape.

Visible-wavelength complex refractive indices of aerosols significantly vary between different chemical compositions of particles. Hygroscopic particles are generally capped and mixed with liquid water in a humid atmosphere. Thus for nearly saturated environment, the refractive index of hygroscopic aerosols becomes close to those of water particles, and creating haze in the atmosphere. Refractive index of mineral dust depends on mineral dust composition [*Nousiainen*, 2009]. The G-SDSU approach, adapted from the R-STAR module, generally utilizes the refractive index derived from the OPAC [*Hess et al*., 1998] and other sources. It should be noted that there are some uncertainties introduced by defining chemical compositions and refractive index from the discrete aerosol categories, since aerosols are often characterized with multiple chemical compositions [*Lesins et al*., 2002].

For either aerosols or hydrometeors, default options of Lorenz-Mie solution with the a priori database of refractive index will give single-scattering efficiencies: extinction efficiency (Q_{ext}), scattering efficiency (Q_{scat}), moments of phase function (P_n), and backscattering efficiency (Q_b). These single-scattering efficiencies are integrated with their PSD function to derive PSD-integrated extinction, single-scattering albedo, and nth moment of phase function:

$$k = \frac{\pi}{4}\int D^2 Q_{\mathrm{ext}} N(D)\mathrm{d}D$$

$$\widetilde{\omega} = \frac{\pi}{4k}\int D^2 Q_{\mathrm{scat}} N(D)\mathrm{d}D$$

$$p_n = \frac{\int D^2 P_n(D) Q_{\mathrm{scat}}(D) N(D)\mathrm{d}D}{\int D^2 Q_{\mathrm{scat}}(D) N(D)\mathrm{d}D}$$

$$\sigma_b = \frac{\int D^2 P_n(D;\Theta=\pi) Q_{\mathrm{scat}}(D) N(D)\mathrm{d}D}{4\pi\int D^2 Q_{\mathrm{scat}}(D) N(D)\mathrm{d}D}$$

Gaseous extinction and absorption are parameterized by the k-distribution method in visible IR spectrum using the HITRAN 2004 database [*Sekiguchi and Nakajima*, 2008] and by empirical fitting parameters in the microwave spectrum [*Rosenkranz*, 1993]. H_2O, CO_2, O_3, N_2O, CO, CH_4, and O_2 are considered over the visible IR spectrum, while H_2O, N_2, and O_2 are considered over microwave spectrum. Because our simulation, in this manuscript, prognoses only water vapor (H_2O), vertical profiles of other gaseous constituent are interpolated at the model pressure levels from climatological values.

Then, for each grid element, bulk single-scattering properties are summed over all gaseous species, hydrometer habits, and aerosol types at frequency ν.

$$k_\nu = \sum k_{\mathrm{gas}} + \sum k_{\mathrm{aer}} + \sum k_{\mathrm{hyd}}$$

$$\widetilde{\omega}_\nu = \frac{1}{k_\nu}\left(\sum k_{\mathrm{gas}}\widetilde{\omega}_{\mathrm{gas}} + \sum k_{\mathrm{aer}}\widetilde{\omega}_{\mathrm{aer}} + \sum k_{\mathrm{hyd}}\widetilde{\omega}_{\mathrm{hyd}}\right)$$

$$p_\nu = \frac{1}{k_\nu\widetilde{\omega}_\nu}\left(\sum k_{\mathrm{gas}}\widetilde{\omega}_{\mathrm{gas}}p_{n,\mathrm{gas}} + \sum k_{\mathrm{aer}}\widetilde{\omega}_{\mathrm{aer}}p_{n,\mathrm{aer}} + \sum k_{\mathrm{hyd}}\widetilde{\omega}_{\mathrm{hyd}}P_{n,\mathrm{hyd}}\right)$$

$$\sigma_\nu = \frac{1}{k_\nu\widetilde{\omega}_\nu}\left(\sum k_{\mathrm{gas}}\widetilde{\omega}_{\mathrm{gas}}\sigma_{\mathrm{gas}} + \sum k_{\mathrm{aer}}\widetilde{\omega}_{\mathrm{aer}}\sigma_{\mathrm{aer}} + \sum k_{\mathrm{hyd}}\widetilde{\omega}_{\mathrm{hyd}}\sigma_{\mathrm{hyd}}\right)$$

Bulk single-scattering properties are separately calculated for the visible IR and microwave spectrums, using the model-consistent PSDs. For example, the visible IR simulator (section 3.1) and the lidar simulator (section 3.4) share an identical method for computing single-scattering properties at visible IR spectrum. The microwave simulator (section 3.2) and the radar simulator (section 3.4) share an identical method for computing single-scattering properties across the microwave spectrum.

Lastly, quantitative uncertainties of the radiance-based evaluation approach are attributed primarily to the uncertainties of the forward models (Modelers must also understand that these uncertainties in the forward model exist in all satellite retrieval algorithms as well.), including computation of single-scattering properties, surface boundary conditions, and RTMs. These forward model components can be improved through close collaboration with the satellite community. Here are, for example, several future improvements list in the G-SDSU:

1. The visible IR simulator: Future improvements include single-scattering properties of nonspherical particles [*Yang et al*., 2005], 3-D effect of radiative transfer at the edge of clouds [*Cahalan et al*., 2005], and surface boundary conditions (albedo and bidirectional reflectance distribution function) for the visible spectrum [*Bicheron and Leroy*, 2000] and surface emissivity for the IR spectrum [*Hulley and Hook*, 2011].
2. The lidar simulator: Future improvements include single-scattering properties of nonspherical particles and realistic representation of depolarization ratio [*Macke et al*., 1996] and multiple-scattering effect of backscatter in the cloud profile [*Hu et al*., 2006].
3. The microwave simulator: Future improvements include single-scattering properties of nonspherical particles at high-frequency channels [*Liu*, 2008] and better dynamic land surface emissivity at low-frequency channels [*Skofronick-Jackson et al*., 2004].
4. The radar simulator: Future improvements include single-scattering properties of nonspherical particles at high-frequency channels [*Okamoto et al*., 1995] and multiple-scattering effect of backscatter (W band) in the deep convective core [*Battaglia et al*., 2008].

These upgrades and their impact on model evaluation are subject to future studies. Single-scattering databases of nonspherical parameters are being incorporated after careful analysis of the observed satellite signals and in situ observations, since neither the satellite nor modeling community can make perfect assumptions in the shapes of nonspherical particles. Fast multiple-scattering models [*Hogan and Battaglia*, 2008] will be incorporated to the lidar and the radar simulator in the future.

Acknowledgments
The work has been supported under NASA Modeling and Analysis Prediction (MAP) program (D. Considine at NASA HQ). is also made to T. Lee at NASA HQ, the NASA Goddard Space Flight Center, and the NASA Ames Research Center for computer resources used for our calculations. Thanks to the anonymous reviewers for improving the manuscript.

References

Aires, F., C. Prigent, and F. Bernardo (2011), A tool to estimate land-surface emissivities at microwave frequencies (TELSEM) for use in numerical weather prediction, *Q. J. R. Meteorol. Soc.*, *137*, 690–699, doi:10.1002/qj.803.

Aonashi, K., and H. Eito (2011), Displaced Ensemble variational assimilation method to incorporate microwave imager brightness temperatures into a cloud-resolving model, *J. Meteorol. Soc. Jpn. Ser. II*, *89*(3), 175–194.

Arkin, P. A., R. Joyce, and J. E. Janowiak (1994), The estimation of global monthly mean rainfall using infrared satellite data: The GOES precipitation index (GPI), *Remote Sens. Rev.*, *11*(1-4), 107–124, doi:10.1080/02757259409532261.

Battaglia, A., J. M. Haynes, T. L'Ecuyer, and C. Simmer (2008), Identifying multiple-scattering-affected profiles in CloudSat observations over the oceans, *J. Geophys. Res.*, *113*, D00A17, doi:10.1029/2008JD009960.

Baum, B. A., P. Yang, A. J. Heymsfield, S. Platnick, M. D. King, Y. X. Hu, and S. T. Bedka (2005), Bulk scattering properties for the remote sensing of ice clouds. Part II: Narrowband models, *J. Appl. Meteorol.*, *44*(12), 1896–1911, doi:10.1175/JAM2309.1.

Berg, W., T. L'Ecuyer, and S. van den Heever (2008), Evidence for the impact of aerosols on the onset and microphysical properties of rainfall from a combination of satellite observations and cloud-resolving model simulations, *J. Geophys. Res.*, *113*, D14S23, doi:10.1029/2007JD009649.

Bicheron, P., and M. Leroy (2000), Bidirectional reflectance distribution function signatures of major biomes observed from space, *J. Geophys. Res.*, *105*(D21), 26,669–26,681, doi:10.1029/2000JD900380.

Bikos, D., et al. (2012), Synthetic satellite imagery for real-time high-resolution model evaluation, *Weather Forecasting*, *27*, 784–795, doi:10.1175/WAF-D-11-00130.1.

Bohren, C. F., and L. J. Battan (1980), Radar backscattering by inhomogeneous precipitation particles, *J. Atmos. Sci.*, *37*, 1821–1827, doi:10.1175/1520-0469(1980)037<1821:RBBIPP>2.0.CO;2.

Bohren, C. F., and D. R. Huffman (1998), *Absorption and Scattering of Light by Small Particles*, 544 pp., Wiley-Vch Verlag GmbH, Weinheim, Germany, doi:10.1002/9783527618156.

Bosilovich, M. G., J. D. Radakovich, A. da Silva, R. Todling, and F. Verter (2007), Skin temperature analysis and bias correction in a coupled land-atmosphere data assimilation system, *J. Meteorol. Soc. Jpn.*, *85*, 205–228, doi:10.2151/jmsj.85A.205.

Burlaud, C., G. Deblonde, and J.-F. Mahfouf (2007), Simulation of satellite passive-microwave observations in rainy atmospheres at the Meteorological Service of Canada, *IEEE Trans. Geosci. Remote Sens.*, *45*(7), 2276–2286, doi:10.1109/MICRAD.2006.1677103.

Cahalan, R. F., L. Oreopoulos, A. Marshak, K. F. Evans, A. B. Davis, R. Pincus, K. H. Yetzer, B. Mayer, R. Davies, and T. P. Ackerman (2005), The I3RC: Bringing together the most advanced radiative transfer tools for cloudy atmospheres, *Bull. Am. Meteorol. Soc.*, *86*(9), 1275–1293, doi:10.1175/BAMS-86-9-1275.

Chaboureau, J.-P., and J.-P. Pinty (2006), Validation of a cirrus parameterization with Meteosat Second Generation observations, *Geophys. Res. Lett.*, *33*, L03815, doi:10.1029/2005GL024725.

Chaboureau, J.-P., J.-P. Cammas, P. Mascart, J.-P. Pinty, C. Claud, R. Roca, and J.-J. Morcrette (2000), Evaluation of a cloud system life-cycle simulated by Meso-NH during FASTEX using METEOSAT radiances and TOVS-3I cloud retrievals, *Q. J. R. Meteorol. Soc.*, *126*, 1735–1750, doi:10.1002/qj.49712656609.

Chaboureau, J.-P., J.-P. Cammas, P. J. Mascart, J.-P. Pinty, and J.-P. Lafore (2002), Mesoscale model cloud scheme assessment using satellite observations, *J. Geophys. Res.*, *107*(D16), 4301, doi:10.1029/2001JD000714.

Chaboureau, J. P., P. Tulet, and C. Mari (2007), Diurnal cycle of dust and cirrus over West Africa as seen from Meteosat Second Generation satellite and a regional forecast model, *Geophys. Res. Lett.*, *34*, L02822, doi:10.1029/2006GL027771.

Chaboureau, J.-P., E. Richard, J.-P. Pinty, C. Flamant, P. Di Girolamo, C. Kiemle, A. Behrendt, H. Chepfer, M. Chiriaco, and V. Wulfmeyer (2011), Long-range transport of Saharan dust and its radiative impact on precipitation forecast: A case study during the Convective and Orographically-induced Precipitation Study (COPS), *Q. J. R. Meteorol. Soc.*, *137*, 236–251, doi:10.1002/qj.719.

Chaboureau, J.-P., O. Nuissier, and C. Claud (2012), Verification of ensemble forecasts of Mediterranean high-impact weather events against satellite observations, *Nat. Hazards Earth Syst. Sci.*, *12*, 2449–2462, doi:10.5194/nhess-12-2449-2012.

Chang, F.-L., and Z. Li (2003), Retrieving vertical profiles of water-cloud droplet effective radius: Algorithm modification and preliminary application, *J. Geophys. Res.*, *108*(D24), 4763, doi:10.1029/2003JD003906.

Chang, F.-L., and Z. Li (2005), A new method for detection of cirrus overlapping water clouds and determination of their optical properties, *J. Atmos. Sci.*, *62*, 3993–4009, doi:10.1175/JAS3578.1.

Cheng, T., Y. Peng, J. Feichter, and I. Tegen (2008), An improvement on the dust emission scheme in the global aerosol-climate model ECHAM5-HAM, *Atmos. Chem. Phys.*, *8*(4), 1105–1117, doi:10.5194/acp-8-1105-2008.

Chevallier, F., and G. Kelly (2002), Model clouds as seen from space: Comparison with geostationary imagery in the 11-μm window channel, *Mon. Weather Rev.*, *130*, 712–722, doi:10.1175/1520-0493(2002)130<0712:MCASFS>2.0.CO;2.

Chin, M., R. B. Rood, S.-J. Lin, J.-F. Müller, and A. M. Thompson (2000), Atmospheric sulfur cycle simulated in the global model GOCART: Model description and global properties, *J. Geophys. Res.*, *105*(D20), 24,671–24,687, doi:10.1029/2000JD900384.

Cintineo, R., J. A. Otkin, M. Xue, and F. Kong (2014), Evaluating the performance of planetary boundary layer and cloud microphysical parameterization schemes in convection-permitting ensemble forecasts using synthetic GOES-13 satellite observations, *Mon. Weather Rev.*, *142*, 163–182, doi:10.1175/MWR-D-13-00143.1.

Clark, A. J., et al. (2012), An overview of the 2010 hazardous weather testbed experimental forecast program spring experiment, *Bull. Am. Meteorol. Soc.*, *93*, 55–74, doi:10.1175/BAMS-D-11-00040.1.

Cotton, W. R., R. A. Pielke Sr., R. L. Walko, G. E. Liston, C. J. Tremback, H. Jiang, R. L. McAnelly, J. Y. Harrington, M. E. Nicholls, and G. G. Carrio (2003), RAMS 2001: Current status and future directions, *Meteorol. Atmos. Phys.*, *82*(1-4), 5–29, doi:10.1007/s00703-001-0584-9.

Dadson, S. J., I. Ashpole, P. Harris, H. N. Davies, D. B. Clark, E. Blyth, and C. M. Taylor (2010), Wetland inundation dynamics in a model of land surface climate: Evaluation in the Niger inland delta region, *J. Geophys. Res.*, *115*, D23114, doi:10.1029/2010JD014474.

Draine, B. T., and P. J. Flatau (1994), Discrete-dipole approximation for scattering calculations, *JOSA A*, *11*(4), 1491–1499, doi:10.1364/JOSAA.11.001491.

Dubovik, O., and M. D. King (2000), A flexible inversion algorithm for retrieval of aerosol optical properties from Sun and sky radiance measurements, *J. Geophys. Res.*, *105*(D16), 20,673–20,696, doi:10.1029/2000JD900282.

Eliasson, S., S. A. Buehler, M. Milz, P. Eriksson, and V. O. John (2011), Assessing observed and modelled spatial distributions of ice water path using satellite data, *Atmos. Chem. Phys.*, *11*, 375–391, doi:10.5194/acp-11-375-2011.

Fraser, A. B., and C. F. Bohren (1992), Is virga rain that evaporates before reaching the ground?, *Mon. Weather Rev.*, *120*(8), 1565–1571, doi:10.1175/1520-0493(1992)1202.0.CO;2.

Gao, W., C.-H. Sui, T.-C. C. Wang, and W.-Y. Chang (2011), An evaluation and improvement of microphysical parameterization from a two-moment cloud microphysics scheme and the Southwest Monsoon Experiment (SoWMEX)/Terrain-influenced Monsoon Rainfall Experiment (TiMREX) observations, *J. Geophys. Res.*, *116*, D19101, doi:10.1029/2011JD015718.

Ginoux, P., M. Chin, I. Tegen, J. M. Prospero, B. Holben, O. Dubovik, and S.-J. Lin (2001), Sources and distributions of dust aerosols simulated with the GOCART model, *J. Geophys. Res.*, *106*(D17), 20,255–20,273, doi:10.1029/2000JD000053.

Grasso, L., and D. Lindsey (2011), An example of the use of synthetic 3.9 μm GOES-12 imagery for two-moment microphysical evaluation, *Int. J. Remote Sens.*, *32*(8), 2337–2350, doi:10.1080/01431161003698294.

Grasso, L., M. Sengupta, and M. Demaria (2010), Comparison between observed and synthetic 6.5 and 10.7 μm GOES-12 imagery of thunderstorms that occurred on 8 May 2003, *Int. J. Remote Sens.*, *31*(3), 647–663, doi:10.1080/01431160902894483.

Grell, G. A., S. E. Peckham, R. Schmitz, S. A. McKeen, G. Frost, W. C. Skamarock, and B. Eder (2005), Fully coupled "online" chemistry within the WRF model, *Atmos. Environ.*, *39*(37), 6957–6975, doi:10.1029/2000JD000053.

Han, M., S. A. Braun, T. Matsui, and C. R. Williams (2013), Evaluation of cloud microphysics schemes in simulations of a winter storm using radar and radiometer measurements, *J. Geophys. Res. Atmos.*, *118*, 1401–1419, doi:10.1002/jgrd.50115.

Hashino, T., M. Satoh, Y. Hagihara, T. Kubota, T. Matsui, T. Nasuno, and H. Okamoto (2013), Evaluating cloud microphysics from NICAM against CloudSat and CALIPSO, *J. Geophys. Res. Atmos.*, *118*, 1–20, doi:10.1002/jgrd.50564.

Hess, M., P. Koepke, and I. Schult (1998), Optical properties of aerosols and clouds: The software package OPAC, *Bull. Am. Meteorol. Soc.*, *79*(5), 831–844, doi:10.1175/1520-0477(1998)079<0831:OPOAAC>2.0.CO;2.

Heymsfield, A. J., and C. M. R. Platt (1984), A parameterization of the particle size spectrum of ice clouds in terms of the ambient temperature and the ice water content, *Atmos. Sci.*, *41*, 846–855, doi:10.1175/1520-0469(1984)041%3C0846:APOTPS%3E2.0.CO;2.

Higurashi, A., and T. Nakajima (1999), Development of a two-channel aerosol retrieval algorithm on a global scale using NOAA AVHRR, *J. Atmos. Sci.*, *56*(7), 924–941, doi:10.1175/1520-0469(1999)056<0924:DOATCA>2.0.CO;2.

Hogan, R. J., and A. Battaglia (2008), Fast lidar and radar multiple-scattering models. Part II: Wide-angle scattering using the time-dependent two-stream approximation, *J. Atmos. Sci.*, *65*(12), 3636–3651, doi:10.1175/2008JAS2643.1.

Hong, S.-Y., and J.-O. J. Lim (2006), The WRF single-moment 6-class microphysics scheme (WSM6), *J. Korean Meteorol. Soc.*, *42*(2), 129–151, doi:10.1002/qj.49712656914.

Hu, Y. (2007), Depolarization ratio–effective lidar ratio relation: Theoretical basis for space lidar cloud phase discrimination, *Geophys. Res. Lett.*, *34*, L11812, doi:10.1029/2007GL029584.

Hu, Y., Z. Liu, D. Winker, M. Vaughan, V. Noel, L. Bissonnette, G. Roy, and M. McGill (2006), Simple relation between lidar multiple scattering and depolarization for water clouds, *Opt. Lett.*, *31*(12), 1809–1811, doi:10.1364/OL.31.001809.

Hufford, G. (1991), A model for the complex permittivity of ice at frequencies below 1 THz, *Int. J. Infrared Millimeter Waves*, *12*, 677–682, doi:10.1007/BF01008898.

Hulley, G. C., and S. J. Hook (2011), Generating consistent land surface temperature and emissivity products between ASTER and MODIS data for Earth science research, *IEEE Trans. Geosci. Remote Sens.*, *49*(4), 1304–1315, doi:10.1109/TGRS.2010.2063034.

Iguchi, T., T. Matsui, J. J. Shi, W. Tao, A. P. Khain, A. Hou, R. Cifelli, A. Heymsfield, and A. Tokay (2012), Numerical analysis using WRF-SBM for the cloud microphysical structures in the C3VP field campaign: Impacts of supercooled droplets and resultant riming on snow microphysics, *J. Geophys. Res.*, *117*, D23206, doi:10.1029/2012JD018101.

Inoue, T. (1987), A cloud type classification with NOAA 7 split-window measurements, *J. Geophys. Res.*, *92*(D4), 3991–4000, doi:10.1029/JD092iD04p03991.

Janowiak, J. E., R. J. Joyce, and Y. Yarosh (2001), A real-time global half-hourly pixel-resolution infrared dataset and its applications, *Bull. Am. Meteorol. Soc.*, *82*(2), 205–217, doi:10.1175/1520-0477(2001)082<0205:ARTGHH>2.3.CO;2.

Kawanishi, T., T. Sezai, Y. Ito, K. Imaoka, T. Takeshima, Y. Ishido, A. Shibata, M. Miura, H. Inahata, and R. W. Spencer (2003), The Advanced Microwave Scanning Radiometer for the Earth Observing System (AMSR-E), NASDA's contribution to the EOS for global energy and water cycle studies, *IEEE Trans. Geosci. Remote Sens.*, *41*(2), 184–194, doi:10.1109/TGRS.2002.808331.

Keil, C., A. Tafferner, H. Mannstein, and U. Schättler (2003), Evaluating high-resolution model forecasts of European winter storms by use of satellite and radar observations, *Weather Forecasting*, *18*, 732–747, doi:10.1175/1520-0434(2003)018<0732:EHMFOE>2.0.CO;2.

Khain, A., D. Rosenfeld, and A. Pokrovsky (2005), Aerosol impact on the dynamics and microphysics of deep convective clouds, *Q. J. R. Meteorol. Soc.*, *131*(611), 2639–2663, doi:10.1256/qj.04.62.

King, M. D., Y. J. Kaufman, W. P. Menzel, and D. Tanre (1992), Remote sensing of cloud, aerosol, and water vapor properties from the Moderate Resolution Imaging Spectrometer (MODIS), *IEEE Trans. Geosci. Remote Sens.*, *30*(1), 2–27, doi:10.1109/36.124212.

Kummerow, C. (1993), On the accuracy of the Eddington approximation for radiative transfer in the microwave frequencies, *J. Geophys. Res.*, *98*, 2757–2765, doi:10.1029/92JD02472.

Kummerow, C., Y. Hong, W. S. Olson, S. Yang, R. F. Adler, J. McCollum, R. Ferraro, G. Petty, D.-B. Shin, and T. T. Wilheit (2001), The evolution of the Goddard Profiling Algorithm (GPROF) for rainfall estimation from passive microwave sensors, *J. Appl. Meteorol.*, *40*(11), 1801–1820, doi:10.1175/1520-0450(2001)040<1801:TEOTGP>2.0.CO;2.

Lang, S., W. K. Tao, J. Simpson, and B. Ferrier (2003), Modeling of convective-stratiform precipitation processes: Sensitivity to partitioning methods, *J. Appl. Meteorol.*, *42*(4), 505–527, doi:10.1175/1520-0450(2003)042<0505:MOCSPP>2.0.CO;2.

Lang, S., W.-K. Tao, R. Cifelli, W. Olson, J. Halverson, S. Rutledge, and J. Simpson (2007), Improving simulations of convective systems from TRMM LBA: Easterly and westerly regimes, *J. Atmos. Sci.*, *64*, 1141–1164, doi:10.1175/JAS3879.1.

Lang, S. E., W.-K. Tao, X. Zeng, and Y. Li (2011), Reducing the biases in simulated radar reflectivities from a bulk microphysics scheme: Tropical convective systems, *J. Atmos. Sci.*, *68*(10), 2306–2320, doi:10.1175/JAS-D-10-05000.1.

Lesins, G., P. Chylek, and U. Lohmann (2002), A study of internal and external mixing scenarios and its effect on aerosol optical properties and direct radiative forcing, *J. Geophys. Res.*, *107*(D10), 4094, doi:10.1029/2001JD000973.

Li, X., W.-K. Tao, T. Matsui, C. Liu, and H. Masunaga (2010), Improving a spectral bin microphysical scheme using long-term TRMM satellite observations, *Q. J. R. Meteorol. Soc.*, *136*, 382–399, doi:10.1002/qj.569.

Lin, Y.-L., R. D. Farley, and H. D. Orville (1983), Bulk parameterization of the snow field in a cloud model, *J. Climate Appl. Meteorol.*, *22*, 1066–1092, doi:10.1175/1520-0450(1983)022<1065:BPOTSF>2.0.CO;2.

Liou, K.-N. (2002), *An Introduction to Atmospheric Radiation*, 2nd ed., vol. 84, 583 pp., Academic Press, Waltham, Mass., ISBN-13: 978-0124514515.

Liu, G. (2004), Approximation of single scattering properties of ice and snow particles for high microwave frequencies, *J. Atmos. Sci.*, *61*(20), 2441–2456, doi:10.1175/1520-0469(2004)061<2441:AOSSPO>2.0.CO;2.

Liu, G. (2008), A database of microwave single-scattering properties for nonspherical ice particles, *Bull. Am. Meteorol. Soc.*, *89*(10), 1563–1570, doi:10.1175/2008BAMS2486.1.

Liu, G., and J. A. Curry (1992), Retrieval of precipitation from satellite microwave measurement using both emission and scattering, *J. Geophys. Res.*, *97*(D9), 9959–9974, doi:10.1029/92JD00289.

Liu, G., J. A. Curry, and R.-S. Sheu (1995), Classification of clouds over the western equatorial Pacific Ocean using combined infrared and microwave satellite data, *J. Geophys. Res.*, *100*(D7), 13,811–13,826, doi:10.1029/95JD00823.

Mace, G. G., Q. Zhang, M. Vaughan, R. Marchand, G. Stephens, C. Trepte, and D. Winker (2009), A description of hydrometeor layer occurrence statistics derived from the first year of merged Cloudsat and CALIPSO data, *J. Geophys. Res.*, *114*, D00A26, doi:10.1029/2007JD009755.

Macke, A., J. Mueller, and E. Raschke (1996), Single scattering properties of atmospheric ice crystals, *J. Atmos.*, *53*, 2813–2825, doi:10.1175/1520-0469(1996)053<2813:SSPOAI>2.0.CO;2.

Mao, K., Z. Qin, J. Shi, and P. Gong (2005), A practical split-window algorithm for retrieving land-surface temperature from MODIS data, *Int. J. Remote Sens.*, *26*(15), 3181–3204, doi:10.1080/01431160500044713.

Masunaga, H., and C. D. Kummerow (2006), Observations of tropical precipitating clouds ranging from shallow to deep convective systems, *Geophys. Res. Lett.*, *33*, L16805, doi:10.1029/2006GL026547.

Masunaga, H., M. Satoh, and H. Miura (2008), A joint satellite and global cloud-resolving model analysis of a Madden-Julian Oscillation event: Model diagnosis, *J. Geophys. Res.*, *113*, D17210, doi:10.1029/2008JD009986.

Masunaga, H., T. Matsui, W.-K. Tao, A. Y. Hou, C. D. Kummerow, T. Nakajima, P. Bauer, W. S. Olson, M. Sekiguchi, and T. Y. Nakajima (2010), Satellite data simulator unit: A multisensor, multispectral satellite simulator package, *Bull. Am. Meteorol. Soc.*, *91*, 1625–1632, doi:10.1175/2010BAMS2809.1.

Matsui, T. (2013), *Chapter 12. Mesoscale Modeling and Satellite Simulator*, *Mesoscale Meteorol. Model.*, 3rd ed., edited by R. A. Pielke Sr., 760 pp., Academic Press, Waltham, Mass., ISBN: 9780123852373.

Matsui, T., A. Beltrán-Przekurat, R. A. Pielke Sr., D. Niyogi, and M. B. Coughenour (2007), Continental-scale multiobservation calibration and assessment of Colorado State University Unified Land Model by application of Moderate Resolution Imaging Spectroradiometer (MODIS) surface albedo, *J. Geophys. Res.*, *112*, G02028, doi:10.1029/2006JG000229.

Matsui, T., X. Zeng, W.-K. Tao, H. Masunaga, W. S. Olson, and S. Lang (2009), Evaluation of long-term cloud-resolving model simulations using satellite radiance observations and multifrequency satellite simulators, *J. Atmos. Oceanic Technol.*, *26*(7), 1261–1274, doi:10.1175/2008JTECHA1168.1.

Matsui, T., et al. (2013), GPM satellite simulator over ground validation sites, *Bull. Am. Meteorol. Soc.*, *94*, 1653–1660, doi:10.1175/BAMS-D-12-00160.1.

Meirold-Mautner, I., C. Prigent, E. Defer, J. R. Pardo, J.-P. Chaboureau, J.-P. Pinty, M. Mech, and S. Crewell (2007), Radiative transfer simulations using mesoscale cloud model outputs: Comparisons with passive microwave and infrared satellite observations for mid-latitudes, *J. Atmos. Sci.*, *64*, 1550–1568, doi:10.1175/JAS3896.1.

Menzel, W. P., R. A. Frey, H. Zhang, D. P. Wylie, C. C. Moeller, R. E. Holz, B. Maddux, B. A. Baum, K. I. Strabala, and L. E. Gumley (2008), MODIS global cloud-top pressure and amount estimation: Algorithm description and results, *J. Appl. Meteorol. Climatol.*, *47*(4), 1175–1198, doi:10.1175/2007JAMC1705.1.

Meyers, M. P., R. L. Walko, J. Y. Harrington, and W. R. Cotton (1997), New RAMS cloud microphysics parameterization. Part II: The two-moment scheme, *Atmos. Res.*, *45*, 3–39, doi:10.1016/S0169-8095(97)00018-5.

Mishchenko, M. I., G. Videen, V. A. Babenko, N. G. Khlebtsov, and T. Wriedt (2004), T-matrix theory of electromagnetic scattering by particles and its applications: A comprehensive reference database, *J. Quant. Spectrosc. Radiat. Transfer*, *88*(1-3), 357–406, doi:10.1016/j.jqsrt.2004.05.002.

Morcrette, J.-J. (1991), Evaluation of model-generated cloudiness: Satellite-observed and model-generated diurnal variability of brightness temperature, *Mon. Weather Rev.*, *119*, 1205–1224, doi:10.1175/1520-0493(1991)119<1205:EOMGCS>2.0.CO;2.

Morrison, H., J. A. Curry, and V. I. Khvorostyanov (2005), A new double-moment microphysics parameterization for application in cloud and climate models. Part I: Description, *J. Atmos. Sci.*, *62*, 1665–1677, doi:10.1175/JAS3446.1.

Myhre, G., F. Stordal, M. Johnsrud, A. Ignatov, M. I. Mishchenko, I. V. Geogdzhayev, D. Tanré, J.-L. Deuzé, P. Goloub, and T. Nakajima (2004), Intercomparison of satellite retrieved aerosol optical depth over the ocean, *J. Atmos. Sci.*, *61*(5), 499–513, doi:10.1175/1520-0469(2004)061<0499:IOSRAO>2.0.CO;2.

Nakajima, T., and M. Tanaka (1986), Matrix formulations for the transfer of solar radiation in a plane-parallel scattering atmosphere, *J. Quant. Spectros. Radiat. Transfer*, *35*(1), 13–21, doi:10.1016/0022-4073(86)90088-9.

Nakajima, T., and M. Tanaka (1988), Algorithms for radiative intensity calculations in moderately thick atmospheres using a truncation approximation, *J. Quant. Spectros. Radiat. Transfer*, *40*(1), 51–69, doi:10.1016/0022-4073(88)90031-3.

Nakajima, T., M. D. King, J. D. Spinhirne, and L. F. Radke (1991), Determination of the optical thickness and effective particle radius of clouds from reflected solar radiation measurements. Part II: Marine stratocumulus observations, *J. Atmos. Sci.*, *48*(5), 728–751, doi:10.1175/1520-0469(1990)047<1878:DOTOTA>2.0.CO;2.

Nakajima, T. Y., K. Suzuki, and G. L. Stephens (2010), Droplet growth in warm water clouds observed by the A-Train. Part I: Sensitivity analysis of the MODIS-derived cloud droplet sizes, *J. Atmos. Sci.*, *67*, 1884–1896, doi:10.1175/2009JAS3280.1.

Njoku, E. G., T. J. Jackson, and V. Lakshmi (2003), Soil moisture retrieval from AMSR-E, *IEEE Trans. Geosci. Remote Sens.*, *41*, 215–229, doi:10.1109/TGRS.2002.808243.

Nousiainen, T. (2009), Optical modeling of mineral dust particles: A review, *J. Quant. Spectros. Radiat. Transfer*, *110*(14), 1261–1279, doi:10.1016/j.jqsrt.2009.03.002.

Okamoto, H., A. Macke, M. Quante, and E. Raschke (1995), Modeling of backscattering by non-spherical ice particles for the interpretation of cloud radar signals at 94 GHz. An error analysis, *Contrib. Atmos. Phys.*, *68*(4), 319–334.

Olson, W. S., P. Bauer, N. F. Viltard, D. E. Johnson, W.-K. Tao, R. Meneghini, and L. Liao (2001a), A melting-layer model for passive/active microwave remote sensing applications. Part I: Model formulation and comparison with observations, *J. Appl. Meteorol.*, *40*(7), 1145–1163, doi:10.1175/1520-0450(2001)040<1145:AMLMFP>2.0.CO;2.

Olson, W. S., Y. Hong, C. D. Kummerow, and J. Turk (2001b), A texture-polarization method for estimating convective-stratiform precipitation area coverage from passive microwave radiometer data, *J. Appl. Meteorol.*, *40*(9), 1577–1591, doi:10.1175/1520-0450(2001)0402.0.CO;2.

Olson, W. S., C. D. Kummerow, S. Yang, G. W. Petty, W.-K. Tao, T. L. Bell, S. A. Braun, Y. Wang, S. E. Lang, and D. E. Johnson (2006), Precipitation and latent heating distributions from satellite passive microwave radiometry. Part I: Improved method and uncertainties, *J. Appl. Meteorol. Climatol.*, *45*(5), 702–720, doi:10.1175/JAM2369.1.

Omar, A. H., D. M. Winker, M. A. Vaughan, Y. Hu, C. R. Trepte, R. A. Ferrare, K.-P. Lee, C. A. Hostetler, C. Kittaka, and R. R. Rogers (2009), The CALIPSO automated aerosol classification and lidar ratio selection algorithm, *J. Atmos. Oceanic Technol.*, *26*(10), 1994–2014, doi:10.1175/2009JTECHA1231.1.

Otkin, J. A., T. J. Greenwald, J. Sieglaff, and H.-L. Huang (2009), Validation of a large-scale simulated brightness temperature dataset using SEVIRI satellite observations, *J. Appl. Meteorol. Climatol.*, *48*, 1613–1626, doi:10.1175/2009JAMC2142.1.

Parkinson, C. L. (2003), Aqua: An Earth-observing satellite mission to examine water and other climate variables, *IEEE Trans. Geosci. Remote Sens.*, *41*(2), 173–183, doi:10.1109/TGRS.2002.808319.

Peters-Lidard, C. D., et al. (2007), High-performance Earth System modeling with NASA/GSFC's Land Information System, *Innovations Syst. Software Eng.*, *3*(3), 157–165, doi:10.1007/s11334-007-0028-x.

Petrenko, M., R. Kahn, M. Chin, A. Soja, and T. Kucsera (2012), The use of satellite-measured aerosol optical depth to constrain biomass burning emissions source strength in the global model GOCART, *J. Geophys. Res.*, *117*, D18212, doi:10.1029/2012JD017870.

Petty, G. W. (2006), *A First Course in Atmospheric Radiation*, 2nd ed., 460 pp., Sundog, Madison, Wis., ISBN-13:978-0-9729033-1-8.

Petty, G. W., and W. Huang (2010), Microwave backscatter and extinction by soft ice spheres and complex snow aggregates, *J. Atmos. Sci.*, *67*(3), 769–787, doi:10.1175/2009JAS3146.1.

Pielke, R. A. (2013), *Mesoscale Meteorological Modeling*, 760 pp., Academic Press, Waltham, Mass., ISBN:9780123852373.

Platt, C. (1973), Lidar and radioinetric observations of cirrus clouds, *J. Atmos. Sci.*, *30*(6), 1191–1204, doi:10.1175/1520-0469(1973)030<1191:LAROOC>2.0.CO;2.

Polkinghorne, R., and T. Vukicevic (2011), Data assimilation of cloud-affected radiances in a cloud-resolving model, *Mon. Weather Rev.*, *139*(3), 755–773, doi:10.1175/2010MWR3360.1.

Price, J. C. (1984), Land surface temperature measurements from the split window channels of the NOAA 7 advanced very high resolution radiometer, *J. Geophys. Res.*, *89*(D5), 7231–7237, doi:10.1029/JD089iD05p07231.

Prigent, C., F. Papa, F. Aires, W. B. Rossow, and E. Matthews (2007), Global inundation dynamics inferred from multiple satellite observations, 1993–2000, *J. Geophys. Res.*, *112*, D12107, doi:10.1029/2006JD007847.

Roebeling, R., B. Baum, R. Bennartz, U. Hamann, A. Heidinger, A. Thoss, and A. Walther (2013), Evaluating and improving cloud parameter retrievals, *Bull. Am. Meteorol. Soc.*, *94*, ES41–ES44, doi:10.1175/BAMS-D-12-00041.1.

Rosenkranz, P. W. (1993), Absorption of microwaves by atmospheric gases, in *Atmospheric Remote Sensing by Microwave Radiometry (A 95-14701 02-46)*, pp. 37–90, John Wiley, New York, ISBN-13: 978-0471628910.

Rossow, W. B., and A. A. Lacis (1990), Global, seasonal cloud variations from satellite radiance measurements. Part II. Cloud properties and radiative effects, *J. Clim.*, *3*(11), 1204–1253, doi:10.1175/1520-0442(1990)003<1204:GSCVFS>2.0.CO;2.

Rossow, W. B., and R. A. Schiffer (1991), ISCCP cloud data products, *Bull. Am. Meteorol. Soc.*, *72*(1), 2–20, doi:10.1175/1520-0477(1991)072<0002:ICDP>2.0.CO;2.

Schoeberl, M. R., A. R. Douglass, E. Hilsenrath, P. K. Bhartia, R. Beer, J. W. Waters, M. R. Gunson, L. Froidevaux, J. C. Gille, and J. J. Barnett (2006), Overview of the EOS Aura mission, *IEEE Trans. Geosci. Remote Sens.*, *44*(5), 1066–1074, doi:10.1109/TGRS.2005.861950.

Seaman, C. J., M. Sengupta, and T. H. Vonder Haar (2010), Mesoscale satellite data assimilation: Impact of cloud-affected infrared observations on a cloud-free initial model state, *Tellus A*, *62*(3), 298–318, doi:10.1111/j.1600-0870.2010.00436.x.

Sekiguchi, M., and T. Nakajima (2008), A k-distribution-based radiation code and its computational optimization for an atmospheric general circulation model, *J. Quant. Spectros. Radiat. Transfer*, *109*(17), 2779–2793, doi:10.1016/j.jqsrt.2008.07.013.

Shi, J. J., T. Matsui, W.-K. Tao, C. Peters-Lidard, M. Chin1, Q. Tan, and E. Kemp (2013), Implementation of an aerosol-cloud microphysics-radiation coupling into the NASA Unified WRF: Simulation results for the 6–7 August 2006 AMMA special observing period, *Q. J. R. Meteorol. Soc.*, doi:10.1002/qj.2286.

Simpson, J., C. Kummerow, W.-K. Tao, and R. F. Adler (1996), On the Tropical Rainfall Measuring Mission (TRMM), *Meteorol. Atmos. Phys.*, *60*(1), 19–36, doi:10.1007/BF01029783.

Skamarock, W. C., et al. (2008), A description of the Advanced Research WRF version 3, *NCAR Tech. Note NCAR/TN-475+STR*, 113 pp., Natl. Cent. for Atmos. Res., Boulder, Colo. [Available online at www.mmm.ucar.edu/wrf/users/docs/arw_v3.pdf.]

Skofronick-Jackson, G. M., M.-J. Kim, J. A. Weinman, and D.-E. Chang (2004), A physical model to determine snowfall over land by microwave radiometry, *IEEE Trans. Geosci. Remote Sens.*, *42*(5), 1047–1058, doi:10.1109/TGRS.2004.825585.

Söhne, N., J.-P. Chaboureau, S. Argence, D. Lambert, and E. Richard (2006), Objective evaluation of mesoscale simulations of the Algiers 2001 flash flood by the model-to-satellite approach, *Adv. Geosci.*, *7*, 247–250, doi:10.5194/adgeo-7-247-2006.

Söhne, N., J.-P. Chaboureau, and F. Guichard (2008), Verification of cloud cover forecast with satellite observation over West Africa, *Mon. Weather Rev.*, *136*, 4421–4434, doi:10.1175/2008MWR2432.1.

Stamnes, K., S.-C. Tsay, K. Jayaweera, and W. Wiscombe (1988), Numerically stable algorithm for discrete-ordinate-method radiative transfer in multiple scattering and emitting layered media, *Appl. Opt.*, *27*(12), 2502–2509, doi:10.1364/AO.27.002502.

Stein, T. H. M., J. Delanoë, and R. J. Hogan (2011), A comparison among four different retrieval methods for ice-cloud properties using data from CloudSat, CALIPSO, and MODIS, *J. Appl. Meteorol. Climatol.*, *50*(9), 1952–1969, doi:10.1175/2011JAMC2646.1.

Stephens, G. L. (1994), *Remote Sensing of the Lower Atmosphere*, 544 pp., Oxford Univ. Press, Oxford, U. K., ISBN-13: 978-0195081886.

Stephens, G. L., D. G. Vane, R. J. Boain, G. G. Mace, K. Sassen, Z. Wang, A. J. Illingworth, E. J. O'Connor, W. B. Rossow, and S. L. Durden (2002), The CloudSat mission and the A-Train: A new dimension of space-based observations of clouds and precipitation, *Bull. Am. Meteorol. Soc.*, *83*(12), 1771–1790, doi:10.1175/BAMS-83-12-1771.

Tanelli, S., S. L. Durden, E. Im, K. S. Pak, D. G. Reinke, P. Partain, J. M. Haynes, and R. T. Marchand (2008), CloudSat's cloud profiling radar after two years in orbit: Performance, calibration, and processing, *IEEE Trans. Geosci. Remote Sens.*, *46*(11), 3560–3573, doi:10.1109/TGRS.2008.2002030.

Tao, W.-K., and M. W. Moncrieff (2009), Multiscale cloud system modeling, *Rev. Geophys.*, *47*, RG4002, doi:10.1029/2008RG000276.

Temimi, M., T. Lacava, I. Coviello, M. Faruolo, R. Khanbilvardi, N. Pergola, V. Tramutoli, and D. Wang (2012), A global passive microwave based wetness index for the monitoring of soil moisture and inundation, Geoscience and Remote Sensing Symposium (IGARSS), 2012 IEEE International(IGARSS), 674-677, doi:10.1109/IGARSS.2012.6351504.

Ulaby, F., R. Moore, and A. Fung (1981), *Microwave Remote Sensing Active and Passing*, *Microwave Remote Sensing Fundamentals and Radiometry*, vol. 1, 456 pp., Addison Wesley, Reading, Mass., ISBN-13: 978-0890061909.

Vukicevic, T., M. Sengupta, A. S. Jones, and T. V. Haar (2006), Cloud-resolving satellite data assimilation: Information content of IR window observations and uncertainties in estimation, *J. Atmos. Sci.*, *63*(3), 901–919, doi:10.1175/JAS3639.1.

Waliser, D., et al. (2009), Cloud ice: A climate model challenge with signs and expectations of progress, *J. Geophys. Res.*, *114*, D00A21, doi:10.1029/2008JD010015.

Walko, R. L., W. R. Cotton, M. P. Meyers, and J. Y. Harrington (1995), New RAMS cloud microphysics parameterization. Part I: the single-moment scheme, *Atmos. Res.*, *38*, 29–62, doi:10.1016/0169-8095(94)00087-T.

Wan, Z., and J. Dozier (1996), A generalized split-window algorithm for retrieving land-surface temperature from space, *IEEE Trans. Geosci. Remote Sens.*, *34*(4), 892–905, doi:10.1109/36.508406.

Weaver, C., et al. (2007), Direct insertion of MODIS radiances in a global aerosol transport model, *J. Atmos. Sci.*, *64*, 808–827, doi:10.1175/JAS3838.1.

Weisman, M. L., W. C. Skamarock, and J. B. Klemp (1997), The resolution dependence of explicitly modeled convective systems, *Mon. Weather Rev.*, *125*, 527–548, doi:10.1175/1520-0493(1997)125<0527:TRDOEM>2.0.CO;2.

Wiedner, M., C. Prigent, J. R. Pardo, O. Nuissier, J.-P. Chaboureau, J.-P. Pinty, and P. Mascart (2004), Modeling of passive microwave responses in convective situations using outputs from mesoscale models: Comparison with TRMM/TMI satellite observations, *J. Geophys. Res.*, *109*, D06214, doi:10.1029/2003JD004280.

Winker, D. M. (2003), Accounting for multiple scattering in retrievals from space lidar, in *Proc. SPIE 5059, 12th International Workshop on Lidar Multiple Scattering Experiments*, pp. 128–139, Oberpfaffenhofen, Germany, doi:10.1117/12.512352.

Winker, D. M., W. H. Hunt, and M. J. McGill (2007), Initial performance assessment of CALIOP, *Geophys. Res. Lett.*, *34*, L19803, doi:10.1029/2007GL030135.

Winker, D. M., M. A. Vaughan, A. Omar, Y. Hu, K. A. Powell, Z. Liu, W. H. Hunt, and S. A. Young (2009), Overview of the CALIPSO mission and CALIOP data processing algorithms, *J. Atmos. Oceanic Technol.*, *26*(11), 2310–2323, doi:10.1175/2009JTECHA1281.1.

Yang, P., H. Wei, H.-L. Huang, B. A. Baum, Y. X. Hu, G. W. Kattawar, M. I. Mishchenko, and Q. Fu (2005), Scattering and absorption property database for nonspherical ice particles in the near-through far-infrared spectral region, *Appl. Opt.*, *44*(26), 5512–5523, doi:10.1364/AO.44.005512.

Yoshida, R., H. Okamoto, Y. Hagihara, and H. Ishimoto (2010), Global analysis of cloud phase and ice crystal orientation from Cloud-Aerosol Lidar and Infrared Pathfinder Satellite Observation (CALIPSO) data using attenuated backscattering and depolarization ratio, *J. Geophys. Res.*, *115*, D00H32, doi:10.1029/2009JD012334.

Zhang, D., Z. Wang, and D. Liu (2010), A global view of midlevel liquid-layer topped stratiform cloud distribution and phase partition from CALIPSO and CloudSat measurements, *J. Geophys. Res.*, *115*, DO0H13, doi:10.1029/2009JD012143.

Zhang, S. Q., M. Zupanski, A. Y. Hou, X. Lin, and S. H. Cheung (2013), Assimilation of precipitation-affected radiances in a cloud-resolving WRF ensemble data assimilation system, *Mon. Weather Rev.*, *141*(2), 754–772, doi:10.1175/MWR-D-12-00055.1.

Zupanski, D., S. Q. Zhang, M. Zupanski, A. Y. Hou, and S. H. Cheung (2011a), A prototype WRF-based ensemble data assimilation system for dynamically downscaling satellite precipitation observations, *J. Hydrometeorol.*, *12*(1), 118–134, doi:10.1175/2010JHM1271.1.

Zupanski, D., M. Zupanski, L. D. Grasso, R. Brummer, I. Jankov, D. Lindsey, M. Sengupta, and M. Demaria (2011b), Assimilating synthetic GOES-R radiances in cloudy conditions using an ensemble-based method, *Int. J. Remote Sens.*, *32*(24), 9637–9659, doi:10.1080/01431161.2011.572094.